A luminescent ruthenium complex modulates amyloid assembly and improves Aβ-associated functional deficits in Alzheimer's disease models

Nur Aininie Yusoh,[1,†] Yun Yan,[2,3,†] Dandan Chen,[1] Abigail Taylor,[4] Yanqiu Gao,[2] Yuhan Chen,[2] Jing Chen,[2,*] Martin R. Gill,[4,*] and Xiaohe Tian,[1,*]

[1]Department of Radiology, Huaxi MR Research Center (HMRRC), Institute of Radiology and Medical Imaging, West China Hospital of Sichuan University, Sichuan University, 610041 Chengdu, Sichuan, China.
[2]Department of Pediatric Surgery and Laboratory of Pediatric Surgery, West China Hospital, Sichuan University, 610041 Chengdu, Sichuan, China
[3]Department of Urology, State Key Laboratory of Biotherapy, West China Hospital, Sichuan University, 610041 Chengdu, Sichuan, China
[4]Department of Chemistry, Faculty of Science and Engineering, Swansea University, SA2 8PP Swansea, UK

* Correspondence: jingchen@scu.edu.cn, m.r.gill@swansea.ac.uk and xiaohe.t@wchscu.cn
† These authors contributed equally to this work.

Abstract

Rationale: Progressive accumulation and propagation of amyloid-β (Aβ) assemblies contribute to neuronal dysfunction and cognitive decline in Alzheimer's disease (AD), yet molecular systems capable of simultaneously targeting amyloid pathology, reporting amyloid recognition, and improving functional outcomes remain limited.

Methods: We developed a series of luminescent ruthenium(II) polypyridyl complexes containing a $[Ru(PIP)_2(N^N)]^{2+}$ (PIP = 2-phenylimidazo[4,5-*f*][1,10]phenanthroline) pharmacophore conjugated to different bidentate N,N-donor ligands and identified a lead dppz-containing complex (dppz = dipyridophenazine) through integrated amyloid aggregation assays, biophysical characterization, molecular simulations, neuronal cell studies, and Aβ-induced zebrafish neurotoxicity studies.

Results: Among the series, complex **4**, $[Ru(PIP)_2(dppz)]^{2+}$, exhibited the most favorable overall profile of amyloid-modulating and biological activities. Complex **4** altered $Aβ_{1-42}$ assembly and reduced fibril formation, inhibited acetylcholinesterase (AChE)-facilitated amyloid aggregation, and exhibited enhanced luminescence in the presence of fibrillar Aβ. Computational analyses suggested interactions with aggregation-prone Aβ regions and the peripheral anionic site of AChE, consistent with the experimental findings. In neuronal models, **4** reduced intracellular Aβ-associated signals, alleviated oxidative stress, preserved mitochondrial function, and improved neuronal survival following Aβ challenge. In an acute Aβ-injected zebrafish model, intracerebral administration of **4** after Aβ exposure resulted in detectable brain-associated complex, reduced Aβ-associated pathology and apoptosis, preserved synaptic markers, and improved locomotor responses and spatial learning performance.

Conclusions: This luminescent ruthenium(II) scaffold combines amyloid recognition, assembly modulation, and optical reporting, linking molecular effects on Aβ aggregation with functional

improvements *in vivo* and providing a chemical approach for investigating and targeting pathogenic amyloid assembly pathways.

Keywords: Alzheimer's disease; Amyloid-β aggregation; Neurodegeneration; Chemical biology; Ruthenium(II) complexes

Introduction

Alzheimer's disease (AD) is characterized by progressive disruption of neuronal networks associated with the accumulation of amyloid-β (Aβ) assemblies [1-4]. Increasing evidence indicates that soluble, assembly-competent Aβ species contribute to early circuit dysfunction, including aberrant neuronal hyperactivity, well before extensive plaque deposition becomes overt [5]. Studies have further revealed that $A\beta_{42}$ forms persistent oligomeric populations that coexist with mature fibrils and may serve as reservoirs of neurotoxic species [6, 7]. These findings suggest that the aggregation landscape itself can act as an active driver of pathology rather than merely a late-stage hallmark, motivating chemical strategies aimed at modulating early assembly processes governed by weak, multivalent hydrophobic, electrostatic and π-driven interactions. Although several therapeutic approaches provide symptomatic relief, interventions that directly control the aggregation behavior of Aβ remain limited. Despite renewed clinical momentum following the approval of anti-Aβ biologics, antibody-mediated clearance operates through mechanisms distinct from small-molecule modulation of aggregation pathways [8, 9]. Whereas immunotherapies primarily promote extracellular peptide removal, chemically defined scaffolds offer the possibility of reshaping aggregation kinetics, altering the balance between soluble and insoluble species, and directly reporting molecular engagement.

High-sensitivity imaging technologies capable of tracking amyloid assemblies could provide valuable feedback for the rational design of therapeutic agents. Among these approaches, fluorescence imaging offers advantages including non-radioactive detection, high sensitivity and real-time observation [10-12]. Fluorescent probes such as thioflavin derivatives - Thioflavin T (ThT) and Thioflavin S (ThS) - have long been used to detect amyloid fibrils *in vitro* and in histological samples. However, most existing probes primarily function as reporters of amyloid deposition and rarely combine detection with the ability to modulate aggregation processes. Recent three-dimensional imaging studies of human cerebral amyloid angiopathy have further demonstrated that Aβ deposition follows complex spatial patterns within vascular networks, emphasizing the importance of understanding amyloid behavior within intact biological environments [13]. At the same time, the free-energy differences separating monomeric, oligomeric and fibrillar states of Aβ are small and distributed across heterogeneous contact surfaces, while fibril polymorphism further complicates selective targeting [14, 15]. Recent high-throughput screening studies have identified chemotypes capable of selectively recognizing distinct fibrillar structures, underscoring the importance of scaffold architecture in determining amyloid binding behavior [16].

Coordination complexes offer a versatile design platform for addressing multifactorial recognition problems, and ruthenium(II) polypyridyl complexes (RPCs) are particularly attractive in this regard [17-19]. RPCs can be tuned for Aβ recognition by varying the size, shape and aromatic surface of their ligands. Their kinetically inert octahedral geometry and extended aromatic ligands enable interactions with biomolecular surfaces through hydrophobic and π-driven

contacts, while the metal centre can influence electronic structure and downstream biological responses. In addition, metal-to-ligand charge-transfer (MLCT) excited states confer intrinsic environment-sensitive luminescence. Photoluminescent Ru(II) systems have been exploited as reporters of amyloid binding [20-23], inhibitors of Aβ aggregation [24, 25], and modulators of α-synuclein [26] while photoactivatable Ru platforms have also been explored to drive oxidative disassembly of aggregates under irradiation [27-29]. However, several recurrent limitations remain, including limited mechanistic studies in neuronal systems and only a single reported example of vertebrate *in vivo* delivery of metal-based therapeutics [30].

Beyond intrinsic peptide self-assembly, accessory proteins can template or accelerate fibrillogenesis. Acetylcholinesterase (AChE) represents a prominent example: its peripheral anionic site (PAS) promotes Aβ assembly, linking cholinergic biology to amyloid formation [31, 32]. Clinically used AChE inhibitors such as donepezil, rivastigmine and galantamine primarily elevate synaptic acetylcholine levels and provide symptomatic benefit, but do not directly address amyloid assembly [33]. The PAS-mediated, non-catalytic role of AChE therefore offers a chemically tractable entry point: ligands occupying the PAS can potentially slow enzyme-accelerated fibril formation while simultaneously engaging aggregation-prone peptide regions through aromatic surface interactions. Achieving both within one scaffold requires matching two distinct surfaces - a structured protein pocket and a dynamic peptide interface - through a common set of non-covalent interactions. While individual strategies targeting Aβ aggregation, enzymatic pathways, or imaging have been explored, their integration within a single metal-based platform with demonstrated *in vivo* functional efficacy remains limited.

To investigate whether a single coordination scaffold could simultaneously recognize and regulate pathogenic Aβ assemblies, we examined a series of Ru(II) polypyridyl complexes of the general formula $[Ru(PIP)_2(N\hat{}N)]^{2+}$, where N^N = bpy (2,2'-bipyridine, **1**), dmb (5,5'-dimethylbpy, **2**), phen (1,10-phenanthroline, **3**), or dppz (**4**). Among these complexes, **4** showed the strongest inhibition of Aβ fibrillogenesis, attenuated AChE-facilitated Aβ aggregation, and exhibited amyloid-responsive luminescence. Molecular modelling indicated that **4** interacts with aggregation-relevant Aβ regions through aromatic and hydrophobic contacts. In neuronal models and Aβ-challenged zebrafish, **4** reduced pathological Aβ-associated changes and improved functional outcomes. To our knowledge, this study provides evidence that a structurally defined metal-based Aβ modulator can couple molecular regulation of amyloid assembly with behavioral recovery in a vertebrate model.

Materials and Methods

Synthesis and characterization of Ru(II) complexes

Complexes **1**, **3**, and **4** were synthesized according to modified literature procedures based on Elgar et al. [34]. Purity and identity were confirmed by $^{1}H/^{13}C$ nuclear magnetic resonance (NMR) spectroscopy, high-resolution mass spectrometry (HRMS), high-performance liquid chromatography (HPLC), Fourier transform infrared (FT-IR) spectroscopy, and elemental analysis. Detailed synthetic procedures and characterization data are provided in the Supplementary Information.

Preparation of amyloid-β species

Lyophilized $A\beta_{1-42}$ (Tocris) or $A\beta_{25-35}$ (MedChemExpress) peptides were pretreated with hexafluoroisopropanol (HFIP, 1 mg mL^{-1}), briefly vortexed, and incubated at room temperature

(RT) for 1 h to disrupt pre-existing aggregates. HFIP was removed to obtain a thin peptide film. The dried film was dissolved in dimethyl sulfoxide (DMSO) to prepare a 1 mM stock, aliquoted and stored at -80 °C. HFIP-treated $A\beta_{1-42}$ (GenicBio) was also used. For aggregation experiments, peptide stocks were diluted in phosphate-buffered saline (PBS, pH 7.4) to the desired concentration. Monomeric Aβ was used immediately after dilution. Oligomeric Aβ was generated by incubation at 4 °C for 24 h without agitation, whereas fibrillar Aβ was formed at 37 °C for 72 h.

Thioflavin T fluorescence assay

Aβ peptides were incubated with Ru(II) complexes, AChE (Sigma-Aldrich), and/or donepezil (MedChemExpress), as specified in the main text. ThT stock solution (1 mM; Sigma-Aldrich) was prepared in ultrapure water and filtered through a 0.22 μm membrane before use. ThT was added to peptide samples at 20 μM and incubated for 15 min at 37 °C. Fluorescence was measured using a BioTek Synergy Mx microplate reader at λ_{ex} = 440 nm and λ_{em} = 490 nm. Emission spectra were collected from 450-650 nm. Measurements were performed in triplicate. Signals were background-subtracted and normalized to the fluorescence intensity of the Aβ-only control, which was set to 100%. Relative aggregation inhibition was calculated from the normalized fluorescence values obtained from three independent experiments. For ThT fluorescence imaging, samples were observed using an Olympus IX73 fluorescence microscope with a 488 nm excitation filter set.

Turbidity assay

Aβ peptides were incubated with Ru(II) complexes as specified in the main text, and aggregation was monitored by absorbance at 405 nm using a Tecan Infinite 200Pro microplate reader for up to 9 days.

Transmission electron microscopy (TEM)

Aβ peptides were incubated with Ru(II) complexes as specified in the main text. A 10 μL aliquot of each incubated sample was deposited onto 300-mesh Formvar-coated copper grids for 3 min, blotted, rinsed twice with ultrapure water, negatively stained with 1% phosphotungstic acid (pH 7.4) for 3 min, rinsed, air-dried at RT and imaged using a Tecnai 12 transmission electron microscope. Aggregate morphology was qualitatively assessed based on fibril abundance, fibril length, and the presence of amorphous aggregates. Representative images from three independent preparations are shown.

Dynamic light scattering (DLS)

Aβ peptides were incubated with Ru(II) complexes as specified in the main text. Samples were gently mixed before analysis using a Malvern Zetasizer Nano ZS90; size distributions were calculated by cumulant analysis using Zetasizer software v7.13.

Bicinchoninic acid (BCA) assay

Aβ peptides were incubated with Ru(II) complexes as specified in the main text. To quantify soluble Aβ, samples (100 μL) were centrifuged at 10,000 rpm for 10 min, and 25 μL of the supernatant was mixed with 200 μL BCA working reagent (Beyotime), incubated at 37 °C for 30 min and read at 562 nm using a Tecan Infinite 200Pro microplate reader.

Molecular docking

Structures of AChE (PDB ID: 1QTI), $A\beta_{1-42}$ (PDB ID: 1IYT) and $A\beta_{25-35}$ (PDB ID: 1QWP) were obtained from the Protein Data Bank. For $A\beta_{1-42}$ docking, the NMR-derived structure (PDB ID: 1IYT) was selected to investigate potential interactions between complexes **1-4** and a monomeric Aβ conformation that may contribute to their aggregation-inhibitory activity. This structure was determined in an aqueous hexafluoroisopropanol environment and adopts a predominantly α-helical conformation [35]. It was therefore used as an experimentally characterized reference structure for comparative docking, rather than as a representation of the conformationally heterogeneous Aβ monomer ensemble or mature fibrils. Proteins were prepared using either the prepare_receptor4 script implemented in MGLTools or PyMOL 2.4 by removing water molecules and co-crystallized ligands, adding polar hydrogens and assigning Gasteiger charges. Structures of **1-4** were generated in GaussView or ChemDraw 20.0 and energy-minimized. The complexes were prepared as PDBQT files using MGLTools/AutoDock Tools 1.5.6. Docking was performed using AutoDock Vina v1.2.5 or v1.1.2. For AChE (PDB ID: 1QTI), docking was centered on the PAS corresponding to the position of the co-crystallized ligand, using a cubic grid box of 35 Å. For Aβ peptides, a blind docking approach was applied using a grid box centered on the geometric center of the peptide (typically 50 Å), or a grid box sufficiently large to fully encompass the peptide structure. For each system, 10-20 docking poses were generated and ranked according to predicted binding energies. The conformation with the lowest predicted binding energy and highest cluster frequency was selected as the most probable binding mode. Docking simulations were repeated three times, and mean docking scores with standard deviations were calculated. Docking results were visualized using PyMOL 2.4 and Discovery Studio 2019 to analyze ligand-protein interactions and binding modes. Selected docking conformations were further subjected to molecular dynamics simulations and structural analysis where indicated.

Molecular dynamics (MD) simulations

MD simulations were performed using GROMACS 2023.2. The AMBER99SB-ILDN force field was applied for the protein, while **4** (ligand) parameters were generated using Sobtop with the General AMBER Force Field (GAFF). The protein-ligand complex was solvated in a cubic TIP3P water box, and counterions were added to neutralize the system. A 1.2 nm cutoff was applied for both van der Waals and short-range electrostatic interactions. Long-range electrostatics were treated using the Particle Mesh Ewald (PME) method. Energy minimization was first performed using the steepest descent algorithm. The system was then equilibrated under NVT conditions for 200 ps followed by NPT equilibration for 100 ps. Temperature was maintained at 303.15 K using the V-rescale thermostat, and pressure was maintained at 1 bar using the Parrinello-Rahman barostat. Production MD simulations were subsequently carried out for 100 ns with a 2-fs time step. Structural stability of the complexes was analyzed by calculating the root-mean-square deviation (RMSD), root-mean-square fluctuation (RMSF), solvent-accessible surface area (SASA), and radius of gyration (Rg) using built-in GROMACS analysis tools.

AChE inhibition assay

AChE inhibition was assessed using a modified Ellman assay. Reactions (200 µL) contained 100 mM phosphate buffer (pH 8.0), 20 µL AChE (0.47 U mL^{-1} in 10 mM phosphate buffer, pH 7.0; Electrophorus electricus Type V-S, Sigma-Aldrich), 20 µL 5,5′ -dithiobis-(2-nitrobenzoic acid) (DTNB) (3.3 mM in 10 mM phosphate buffer, pH 7.0, containing 6 mM sodium bicarbonate ($NaHCO_3$, Sigma-Aldrich)), and 20 µL Ru(II) inhibitor or donepezil solution. Ru complexes were diluted from DMSO stocks, with final DMSO ≤0.5%. Mixtures were preincubated at 37 °C for 20

min before adding 20 µL acetylthiocholine iodide (3.0 mM, Sigma-Aldrich). Absorbance at 412 nm was monitored for 5 min using a Tecan Infinite 200Pro reader. Enzyme-free blanks and inhibitor control wells were included. IC_{50} values were obtained by nonlinear regression.

Dot blot analysis

Aβ peptides (20 µM) were incubated in PBS with or without **4** (10 µM) or AChE at 37 °C for 72 h. Samples (2 µL) were spotted onto methanol-activated PVDF membranes and dried for 15 min at RT. Membranes were blocked with 5% non-fat milk in Tris Buffered Saline with Tween 20 (TBST) for 1 h, incubated overnight at 4 °C with A11 or OC primary antibodies, washed three times with TBST, and incubated with HRP-conjugated secondary antibody for 1 h at RT. After washing, signals were developed using Immobilon Western Chemiluminescent HRP substrate and imaged using a ChemiDoc MP system. Antibody details are listed in the Supplementary Information.

Fluorescence spectroscopy

For photophysical characterization, excitation and emission spectra of **4** (10 µM) were recorded in 0.1% DMSO/H_2O; excitation spectra were collected with emission monitored at 600 nm, and emission spectra were obtained using 450 nm excitation. Absorbance spectra were recorded using a UV-visible spectrophotometer. For fluorescence spectroscopy of amyloid binding, **4** (1 µM) was incubated with monomeric, oligomeric, or fibrillar Aβ species (5 µM) in PBS. Fluorescence spectra were recorded with excitation at 450 nm and emission from 500-800 nm. Concentration-dependent binding was assessed using **4** (1 µM) with Aβ fibrils (0-5 µM). For binding specificity experiments, **4** (1 µM) was incubated with α-synuclein (Abcam), bovine serum albumin (BSA; MedChemExpress), or human serum albumin (HSA; MedChemExpress) in PBS. All measurements were performed at RT in three technical replicates.

Cell culture and neuronal differentiation

SH-SY5Y and HT22 cells were cultured in Dulbecco's Modified Eagle Medium (DMEM) containing 10% fetal bovine serum (FBS) and 1% penicillin-streptomycin at 37 °C with 5% carbon dioxide (CO_2). BV2 cells were maintained in minimum essential medium (MEM) containing nonessential amino acids (NEAA), 2 mM L-glutamine, 2,200 mg/L $NaHCO_3$, and 1,000 mg/L D-glucose, without HEPES, supplemented with 10% FBS and 1% penicillin-streptomycin at 37 °C with 5% CO_2. SH-SY5Y differentiation was induced with retinoic acid (20 µM; MedChemExpress) in DMEM containing 2% FBS for 72 h. Ru(II) compounds were diluted in DMEM, with final DMSO at 0.1%.

MTT assay

Cells were seeded in 96-well plates and treated as described in the main text. Medium was replaced with 3-(4,5-dimethylthiazol-2-yl)-2,5-diphenyltetrazolium bromide (MTT, 0.5 mg mL^{-1}; Sigma-Aldrich) for 3 h at 37 °C, formazan crystals were dissolved in 100 µL DMSO, and absorbance was measured at 570 nm with reference at 620 nm. Viability was calculated relative to untreated controls, and half-maximal inhibitory concentration (IC_{50}) values were fitted in GraphPad Prism.

Cellular uptake

Cells were seeded in Ibidi µ-dishes for 24 h, treated with Ru complexes (25 µM) for 1 h, washed twice with PBS, fixed with 4% paraformaldehyde (PFA) for 10 min at RT, stained with 4’,6-

diamidino-2-phenylindole (DAPI, 0.5 μg mL^{-1}) for 5 min and imaged using a Zeiss LSM 980 confocal laser scanning microscope (CLSM) or structured illumination microscopy (SIM). Ru complexes were excited at 488 nm, and emission was collected at 580-700 nm, with detection windows adjusted to minimize overlap. Images were analyzed using ZEN or ImageJ.

Immunofluorescence staining

Cells were seeded in Ibidi μ-dishes and treated as described in the main text. Cells were then fixed with 4% PFA for 15 min, permeabilized with 0.1% Triton X-100 in PBS for 10 min on ice, blocked with 3% BSA in PBS-T for 1 h, and incubated overnight at 4 °C with primary antibodies. Cells were washed three times with PBS-T, incubated with secondary antibodies for 1 h at RT in the dark, counterstained with DAPI or Hoechst 33342 (5 μg mL^{-1}), and imaged using a Zeiss LSM 980 or Olympus fluorescence microscope IX83. For complex **4** imaging, cells were incubated with **4** (25 μM, 1 h) before nuclear staining. At least 200 nuclei were counted per independent experiment. Images were analyzed using ZEN or ImageJ. Antibody details are listed in the Supplementary Information.

APP/PS1 mouse brain section staining

Paraffin-embedded brain sections from 12-month-old APP/PS1 mice and age-matched wild-type controls were deparaffinized in xylene, rehydrated through ethanol gradients to PBS, fixed with 4% PFA for 15 min, permeabilized with 0.1% Triton X-100 for 10 min, and treated with 0.1 M glycine for 15 min to reduce background. Sections were blocked with 3% BSA for 1 h, incubated overnight at 4 °C with anti-Aβ antibody, washed and incubated with goat anti-rabbit secondary antibody for 1 h at RT. For Ru(II) staining, **4** was applied for 60 min. Where indicated, sections were stained with 0.1% ThS in 50% ethanol for 30 min, briefly differentiated in 80% ethanol, rinsed, mounted with antifade medium and imaged using Zeiss LSM 980. Image processing and analysis were performed using Zeiss ZEN software.

Clonogenic survival assay

Cells were seeded in 6-well plates, treated as described in the main text, switched to drug-free medium and grown for 7-14 days. Colonies were fixed with 100% cold methanol for 20 min at 4 °C and stained with 0.5% crystal violet for 20 min. Excess stain was removed by washing with water. Colony images were captured using a digital imaging system, and colonies were quantified using ImageJ software. The surviving fraction was calculated relative to untreated control cells.

Live/dead staining

Cells were seeded in 6-well plates and treated as described in the main text. Cells were stained with a calcein-AM/PI kit (Beyotime) for 20 min at 37 °C in the dark, washed and imaged using Olympus IX73. Images were analyzed using ImageJ.

ThT staining of intracellular Aβ

Cells were seeded in 6-well plates and treated as described in the main text. Cells were washed with PBS, stained with ThT (20 μM in PBS) for 15 min at RT in the dark, washed, counterstained with Hoechst 33342 and imaged using the FITC channel of a Zeiss LSM 980 microscope. ThT fluorescence intensity was quantified using ImageJ.

Determination of Intracellular ROS levels

Cells were seeded in 6-well plates and treated as described in the main text. Cells were incubated with DCFH-DA (10 μM; Solarbio) in serum-free medium for 60 min at 37 °C in the dark, washed three times and imaged using Olympus IX73; N-acetylcysteine (NAC; 5 mM; MedChemExpress) was used where indicated. Intracellular ROS levels were quantified using ImageJ software.

Measurement of mitochondrial membrane potential (TMRM)

Cells were seeded in 6-well plates and treated as described in the main text. Cells were then stained with tetramethylrhodamine methyl ester (TMRM) (200 nM; Invitrogen) in serum-free medium for 30 min at 37 °C in the dark, washed with PBS, counterstained with Hoechst 33342 and imaged using Olympus IX73. Changes in mitochondrial membrane potential were quantified by measuring TMRM fluorescence intensity using ImageJ software.

Immunoblotting

For cellular studies, cells (1×10^6 per 60 mm dish) were treated as described in the main text and lysed in RIPA buffer supplemented with protease and phosphatase inhibitors. Protein concentrations were determined using a BCA assay. Proteins (40 μg per lane) were separated on 4-20% Mini-PROTEAN TGX SDS–PAGE gels and transferred to methanol-activated PVDF membranes. Membranes were blocked with 5% skimmed milk in Tris-buffered saline containing Tween 20 (TBST) for 1 h, incubated overnight at 4 °C with primary antibodies, washed, and incubated with HRP-conjugated secondary antibodies for 1 h at room temperature. Signals were developed using Immobilon Western chemiluminescent substrate and imaged using a ChemiDoc MP system. Band intensities were quantified using ImageJ after background subtraction. Protein expression levels were normalized to β-actin and expressed relative to the untreated control group. For apoptosis-related proteins, Bax/Bcl-2 and cleaved/full-length protein ratios were calculated where indicated. For Aβ aggregation analysis, $A\beta_{1\text{-}42}$ peptides (20 μM) were incubated with Ru(II) complexes (10 μM) as described in the main text. Following incubation, samples were separated by SDS-PAGE and Aβ species were detected by immunoblotting using the 6E10 primary antibody. Antibody details are provided in the Supplementary Information.

ELISA

The levels of tumor necrosis factor-α (TNF-α) and interleukin-1β (IL-1β) in BV2 microglial cell culture supernatants were quantified using commercially available ELISA kits (Invitrogen, Thermo Fisher Scientific, USA). BV2 cells were treated with Aβ, **4**, or their combination for 24 h. Following treatment, the culture supernatants were collected, and cytokine concentrations were determined according to the manufacturer's instructions.

Zebrafish experiments

Zebrafish husbandry and larval intracerebral injection

Wild-type AB strain zebrafish were maintained at West China Hospital, Sichuan University, at 28 ± 0.5 °C under a 14 h light/10 h dark cycle, following previously described husbandry procedures [36]. Larvae were maintained in Holtfreter's buffer. Anaesthesia was induced using 0.02% (w/v) tricaine (MS-222) prepared in Holtfreter's buffer until loss of response to tactile stimuli. All animal experiments were conducted in accordance with institutional ethical guidelines and approved by the Animal Ethics Committee of West China Hospital, Sichuan University (approval no. 20220422003).

Intracerebral microinjection in zebrafish larvae

Three-day-post-fertilization larvae were anesthetized, positioned on a 1% low-melting agarose template in Holtfreter's buffer, and injected using a calibrated glass microneedle connected to an MPPI-3 pneumatic microinjection system under a stereomicroscope. HiLyte Fluor 647-labelled $A\beta_{1-42}$ (Anaspec) was dissolved in DMSO and diluted in PBS to 50 μM immediately before injection. $A\beta_{1-42}$ solution (5 nL, 50 μM) was injected into the cerebroventricular space through the dorsal tissue at the right optic tectum of the larval brain, with a penetration depth of less than 0.3 mm and injection pressure at 20 psi. Larvae were recovered in fresh Holtfreter's buffer at 28 °C. For biodistribution studies, **4** (5 nL, 1 mM in 1% DMSO) was injected intracerebrally and assessed at 1, 72 and 120 h. Due to its limited aqueous solubility, complex **4** was initially dissolved in DMSO and subsequently diluted with PBS immediately before injection to obtain a final concentration of 1 mM complex **4** in 1% (v/v) DMSO. For treatment and colocalization studies, larvae were first injected with $A\beta_{1-42}$ monomers (5 nL, 50 μM) or PBS. Four hours later, PBS-injected larvae received vehicle, while Aβ-injected larvae received vehicle or **4** (5 nL, 1 mM), generating PBS, Aβ and Aβ + **4** groups. The vehicle contained the same DMSO concentration and buffer composition as the complex **4** injection solution. The 4 h interval allowed an initial period of Aβ exposure before treatment. Larvae were maintained at 28 °C throughout the experiment for subsequent analysis. Prior to the main experiments, the tolerability of the injection conditions was evaluated over seven days. No mortality or obvious morphological abnormalities, including edema, were observed under the conditions tested.

Zebrafish live imaging

Whole-mount confocal imaging was performed using an Olympus FV3000 microscope with a 10× objective. Larvae were anesthetized, mounted in 1% low-melting agarose on glass-bottom dishes, and imaged at RT. Z-stacks were acquired at 5 μm intervals. The same larvae were recovered and re-imaged at subsequent time points. HiLyte Fluor 647-labelled Aβ was imaged using 640 nm excitation and far-red emission; **4** was excited at 488 nm and collected at 580-640 nm with adjusted detection windows. Identical microscope settings were used within each experiment. Images were analyzed using FV3000 software, OlyVIA, ImarisViewer v11.0.0 or ImageJ. For quantitative analysis, identical acquisition parameters and intensity thresholds were applied within each experiment. Fluorescence-positive areas were segmented using a fixed threshold and quantified as the area occupied by detectable fluorescence signal. Each group contained 10 larvae, and the experiments were repeated twice.

ICP-MS analysis of ruthenium accumulation

Larvae were anesthetized with 0.02% tricaine and rinsed twice with PBS. Heads were dissected, and 10 heads were pooled per sample in acid-washed LoBind tubes, weighed, and snap-frozen in liquid nitrogen. Samples were digested in trace-metal-grade HNO_3 (65-70%; approximately 10 μL mg^{-1} tissue) at 65-70 °C for 4 h, diluted to 1 mL with ultrapure water, and centrifuged at 14,000 rpm for 10 min. Ruthenium concentrations were determined using an Agilent 7700 ICP-MS calibrated with external ruthenium standards. For each experimental group, two independently prepared pooled samples were analyzed, each comprising 10 larval heads (n = 2 pooled samples; 20 larvae in total). The ruthenium content of each pooled sample was normalized to its constituent 10 larval heads and expressed as the average ruthenium content per larval head (ng/head). The two

independently prepared pooled samples were used to calculate the group mean and standard deviation.

Behavioral analysis of zebrafish larvae

Larval locomotor behavior was assessed at 3 and 5 days post-injection using a DanioVision behavioral chamber (Noldus Information Technology) and EthoVision XT (Noldus). Individual larvae were placed in 48-well plates containing Holtfreter's buffer. Spontaneous locomotion was recorded for 1 h. Stimulus-evoked locomotion was recorded during mechanical tapping stimulation (1 tap every 5 s) for 10 min. Total distance travelled, mean swimming speed, and movement duration were extracted using EthoVision XT software. Raw tracking data were automatically processed using identical detection settings across all groups. Representative trajectories were generated from individual larvae selected from the corresponding experimental cohort. PBS-injected fish controlled for injection effects. Each experimental condition included 10 larvae per group and was tested in two independent experiments.

Measurement of ROS of zebrafish larvae

Larval heads were collected at 5 days post-injection, homogenized at 70 Hz for 5 min, adjusted to 100 μL with PBS and incubated with DCFH-DA (0.1 μM). Fluorescence was measured at λ_{ex} = 495 nm and λ_{em} = 529 nm, background-subtracted and normalized to untreated controls.

Whole-mount immunofluorescence

Larvae were fixed in 4% PFA overnight at 4 °C, washed three times with PBS-T (PBS containing 0.1% Triton X-100) (5 min each), dehydrated through 25-100% methanol in PBS-T, rehydrated in PBS-T concentration gradient, depigmented with 3% H_2O_2/0.5% potassium hydroxide (KOH) for 30 min at 37 °C, washed three times with PBS-T (5 min each), permeabilized with proteinase K (20 μg mL^{-1}), washed three times with PBS-T (5 min each), blocked with 5% BSA in PBS-T for 1 h and incubated overnight at 4 °C with anti-synaptophysin or anti-Aβ antibodies, washed three times with PBS-T (5 min each), followed by incubation with Alexa Fluor 594-conjugated secondary antibodies for 2 h at RT, washed three times with PBS-T (5 min each). Samples were mounted and imaged using Olympus FV3000 with 10× objective and 5 μm z-stacks. Experiments included at least two independent biological replicates.

TUNEL imaging

Larvae were fixed, methanol-dehydrated, rehydrated, permeabilized with proteinase K (20 μg mL^{-1}), incubated with TUNEL reaction mixture (US Everbright) for 2 h at 37 °C in the dark, washed, counterstained with DAPI (5 μg mL^{-1}) and imaged using Olympus FV3000 with 5 μm z-stacks. Where applicable, co-staining was performed using overnight incubation with primary antibodies followed by fluorescent secondary antibodies. TUNEL-positive nuclei were quantified from maximum-intensity projections of confocal z-stacks using ImageJ. At least three fields of view were analyzed per larva, and the mean value was used for statistical analysis.

Adult zebrafish injection

Adult zebrafish (3-4 months) were anesthetized in 0.02% tricaine for ~20 s until loss of response to tactile stimuli. A ~200 μm skull slit was made in the skull over the optic tectum of the brain, and a glass capillary needle was inserted to inject solution into the cerebroventricular fluid using an MPPI-3 microinjector under a stereomicroscope. Aβ solution (0.1 μL, 500 μM in PBS) was

injected to establish the model and dispersed rostrally toward the forebrain. Complex **4** (0.1 μL, 2 mM) or vehicle was administered 4 h later using the same procedure. Following injection, fish were recovered in fresh system water at 28 °C.

Adult behavioral and cognitive assessment

Adult behavior was assessed at 7 and 14 days post-injection. Locomotion was recorded in a 1 L tank using DanioVision/EthoVision, and distance travelled, swimming velocity and trajectories were analyzed. For T-maze testing, fish were trained twice daily in a maze with one food-baited target arm. Each trial lasted 6 min; a food reward was given after entry into the target arm and a stay of ≥30 s. If no entry occurred within 6 min, fish were guided to the target arm for 3 min of reward exposure. For fish that did not enter the target arm during the 6-min trial, latency was recorded as 360 s. Latency to first entry into the target arm, cumulative time spent in the target arm and number of target-arm entries were measured. Each group contained six adult zebrafish tested at the same time of day under identical lighting conditions. Experiments were repeated three times.

Statistical analysis

Data are presented as mean ± standard deviation (SD) unless otherwise indicated. Statistical analyses were performed using GraphPad Prism 9. Comparisons among multiple groups were performed using one-way ANOVA followed by Tukey's multiple-comparison test unless otherwise stated. Sample sizes (n) represent independent biological replicates and are indicated in the corresponding figure legends. $P < 0.05$ was considered statistically significant.

Results

Identification of a ruthenium complex that suppresses Aβ assembly

To investigate how ligand structure influences Aβ assembly modulation, we examined four structurally related Ru(II) polypyridyl complexes (**1-4**) sharing the $[Ru(PIP)_2(N^N)]^{2+}$ pharmacophore (Figure 1A). Complexes **1-4** incorporate bpy, dmb, phen, and dppz ligands at the N^N position, respectively, allowing us to examine how differences in ligand structure influence amyloid recognition and assembly modulation. Complex **2** was reported previously [34], whereas the novel complexes **1**, **3**, and **4** were synthesized and characterized by NMR spectroscopy, HRMS, elemental analysis, HPLC, and FT-IR spectroscopy (Figures S1-S15). Photophysical characterization revealed characteristic MLCT absorption bands in the visible region (Tables S1 and S2). **1-4** were luminescent in both acetonitrile and water, with distinctive large Stokes shift values (>140 nm) and lifetimes (>100 ns) indicative of MLCT phosphorescence (Tables S1 and S2).

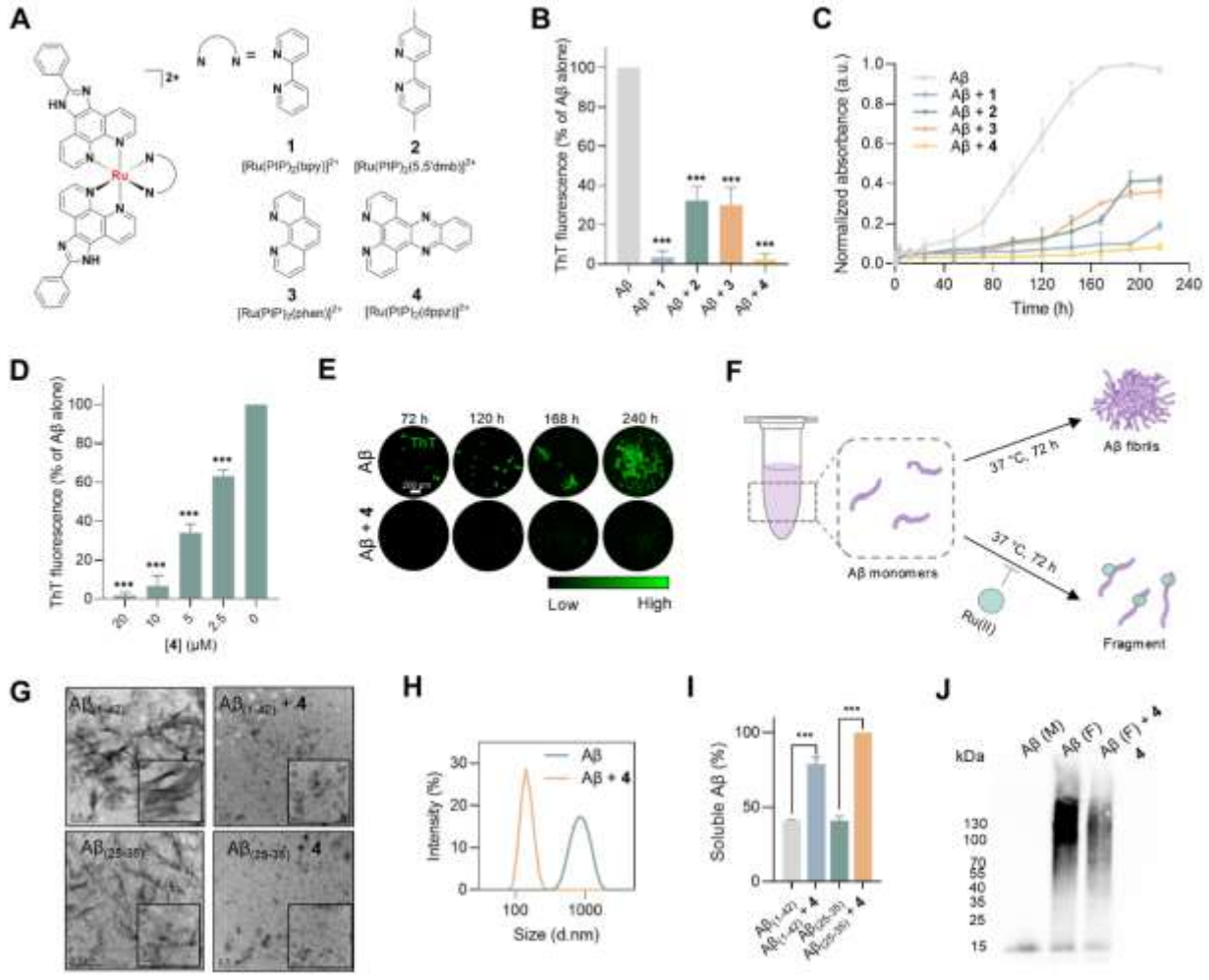

Figure 1. Identification of a ruthenium scaffold that modulates Aβ assembly. (**A**) Chemical structures of **1-4**. **(B)** ThT fluorescence of $A\beta_{1-42}$ incubated with **1-4** (20 μM Aβ, 10 μM Ru complex, 72 h), normalized to Aβ alone (100%) after background subtraction. **(C)** Turbidity of $A\beta_{1-42}$ incubated with or without **1-4** (20 μM Aβ, 10 μM Ru complex, 216 h). **(D)** Concentration-dependent effects of **4** on $A\beta_{1-42}$ ThT fluorescence (20 μM Aβ). **(E)** Representative ThT fluorescence images of $A\beta_{25-35}$ aggregates formed with or without **4** (50 μM Aβ, 10 μM **4**, 72 h). Scale bar, 200 μm. **(F)** Schematic of Aβ assembly modulation by **1-4**. **(G)** TEM images of $A\beta_{1-42}$ and $A\beta_{25-35}$ assemblies formed with or without **4** (20 μM Aβ, 10 μM **4**, 72 h). Scale bars, 0.5 μm; insets, 100 nm. **(H)** DLS analysis of $A\beta_{1-42}$ assemblies with or without **4** after 72 h. **(I)** Soluble $A\beta_{1-42}$ and $A\beta_{25-35}$ fractions after 72 h with or without **4**, quantified by BCA assay. **(J)** Representative 6E10 Western blot of $A\beta_{1-42}$ incubated in PBS with or without **4** for 72 h. Data are mean ± s.d. from three independent experiments, each with three technical replicates. *P < 0.05, **P < 0.01 and ***P < 0.001 versus Aβ alone (**B**) or 0 μM **4** (**D**), one-way ANOVA.

A ruthenium complex suppresses Aβ fibrillogenesis

ThT fluorescence assays were used to examine the effects of **1-4** on Aβ assembly, following approaches previously employed to investigate Ru(II)-mediated modulation of Aβ aggregation [24, 25]. All four complexes reduced ThT fluorescence relative to the Aβ-only control, with **4** producing the greatest reduction, corresponding to 2.55% of the Aβ-only fluorescence intensity (Figure 1B and Figure S16). The characteristic ThT emission profile was retained in the presence of the complexes. Control measurements showed a slight decrease in ThT fluorescence upon addition of **4** in the absence of Aβ, although the difference was not statistically significant, suggesting limited optical interference under these conditions. Turbidity measurements over nine days further revealed reduced light scattering in samples treated with **4** compared to untreated Aβ at day 9 (Figure 1C). Moreover, ThT fluorescence decreased in a concentration-dependent manner upon treatment with **4**, with the fluorescence intensity reduced to 6.78% of the Aβ-only control at 10 μM (Figure 1D). The difference in residual fluorescence between the initial comparison of complexes **1-4** (Figure 1B) and the concentration-dependent experiment (Figure 1D) reflects measurements obtained from separate experimental sets, both showing substantial attenuation of ThT fluorescence at 10 μM. Fluorescence imaging further showed fewer ThT-positive aggregates following treatment with **4** (Figure 1E).

Additionally, TEM revealed extensive fibrillar networks in untreated samples, whereas treatment with **4** resulted in shorter, fragmented, and morphologically heterogeneous assemblies of both $A\beta_{1\text{-}42}$ and $A\beta_{25\text{-}35}$ (Figure 1G). Consistent with these observations, DLS indicated a shift toward smaller apparent particle sizes following treatment with **4** (Figure 1H). Soluble-fraction analysis further showed increased retention of soluble peptide species, with soluble $A\beta_{1\text{-}42}$ and $A\beta_{25\text{-}35}$ levels increasing from 41.05% to 78.93% and from 40.96% to 100%, respectively, following treatment with **4** (Figure 1I). These complementary findings support an effect of **4** on Aβ assembly and fibril formation, identifying it as the lead aggregation modulator within the series. The effect of **4** on Aβ assembly was further examined by Western blotting using the Aβ-specific 6E10 antibody, as previously employed to investigate Ru(II)-mediated modulation of Aβ aggregation [27, 29]. Aβ alone exhibited a broad distribution of 6E10-reactive species extending into the high-molecular-weight region, whereas treatment with **4** reduced the signal associated with these species (Figure 1J). These findings further support changes in the distribution of Aβ assemblies detectable following Western blot, consistent with the TEM, DLS and soluble-fraction analyses.

Computational analysis suggests interactions of 4 with aggregation-prone Aβ regions

To investigate whether the aggregation-inhibitory activity of complexes **1-4** could be associated with their interactions with monomeric Aβ, comparative molecular docking was performed using an experimentally characterized $A\beta_{1\text{-}42}$ conformation (PDB ID: 1IYT), followed by 100-ns MD simulations of **4** with $A\beta_{1\text{-}42}$. Docking calculations yielded predicted binding scores of -7.0, -7.3, -7.4, and -7.4 kcal mol^{-1} for **1-4**, respectively (Figures 2A and S17). A similar trend was observed for the shorter $A\beta_{25\text{-}35}$ fragment (PDB ID: 1QWP), with corresponding scores of -3.9, -3.9, -4.1, and -4.3 kcal mol^{-1} (Figures 2B and S18). Although the differences in docking scores were relatively small, the predicted interaction profiles varied across the series. As PDB 1IYT represents a predominantly α-helical $A\beta_{1\text{-}42}$ conformation determined in an aqueous hexafluoroisopropanol environment, these findings were interpreted as potential interactions with the selected monomeric structure rather than definitive binding modes of Aβ in physiological solution. For $A\beta_{1\text{-}42}$, the complexes interacted predominantly through van der Waals and hydrophobic contacts, while **4** additionally showed π-associated interactions involving His13, together with nonpolar contacts

involving Leu17, Phe20, Ala21 and Val24. In the $A\beta_{25-35}$ model, the predicted interactions were mainly associated with nonpolar residues, including Ile31 and Leu34, with **4** showing the most favorable docking score within the series. These findings suggest that the extended aromatic framework of **4** may facilitate interactions with the selected Aβ structures.

Subsequent MD simulations showed that **4** remained associated with the peptide throughout the 100-ns trajectory, without an apparent dissociation event (Figure 2C). Residue-level flexibility analysis indicated reduced fluctuations in portions of the central hydrophobic region, while the terminal regions remained comparatively dynamic (Figure S19A). A modest decrease in the radius of gyration was observed (Figure S19B), accompanied by relatively limited changes in solvent-accessible surface area (Figure S19C). These observations suggest localized conformational changes rather than extensive structural compaction. Hydrogen-bond analysis further revealed transient hydrogen-bonding interactions during the simulation, alongside the predicted hydrophobic and π-associated contacts (Figure S19D). MM/GBSA analysis identified His13, Leu17, and Met35 as important contributors to the calculated ligand-peptide interaction energy (Figure 2D,E). Overall, the docking and MD results suggest that the extended aromatic framework of **4** may provide additional opportunities for interactions with Aβ, although the small differences in docking scores do not establish substantial differences in binding affinity or fully explain the experimental aggregation-modulating activity.

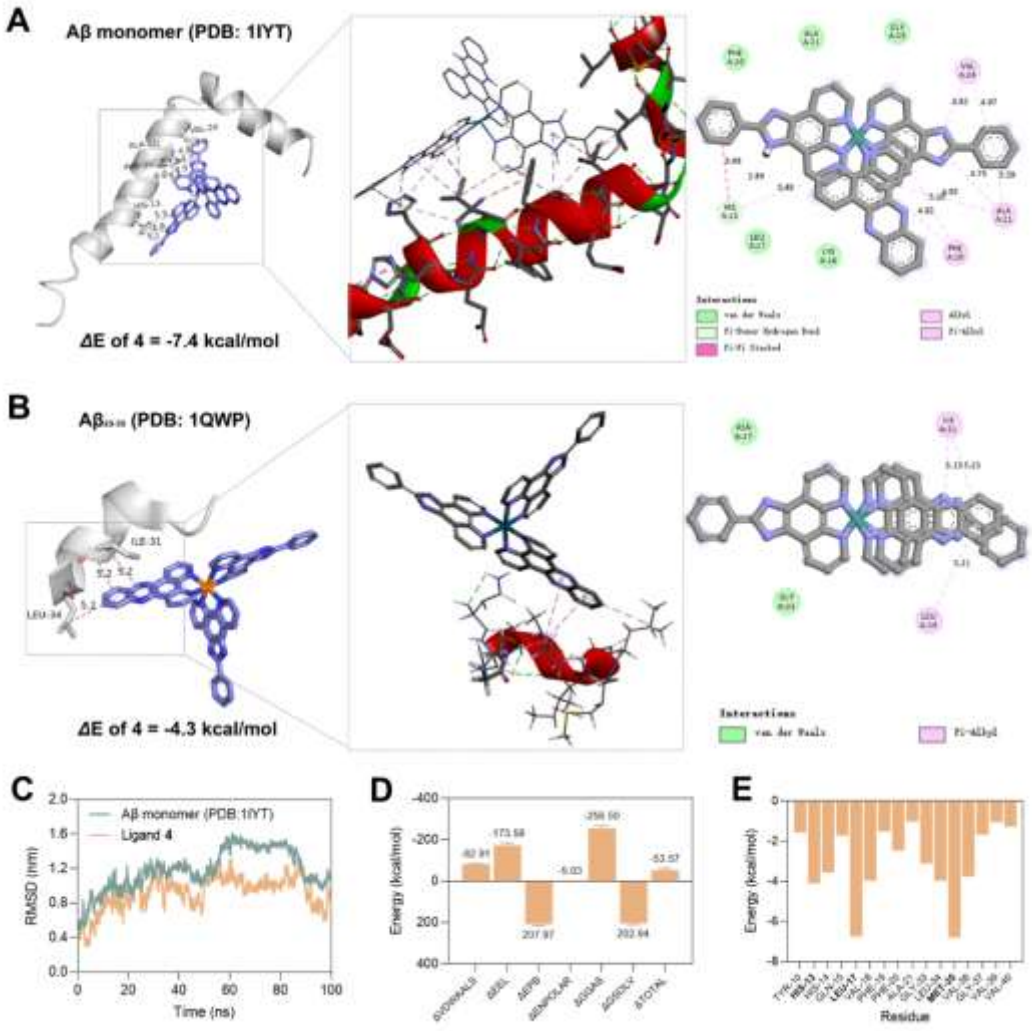

Figure 2. Computational analysis of 4 interactions with aggregation-prone Aβ regions. (**A**) Representative molecular docking pose of **4** with $A\beta_{1\text{-}42}$ (PDB ID: 1IYT). Left, predicted binding pose; right, key intermolecular interactions. (**B**) Representative molecular docking pose of **4** with $A\beta_{25\text{-}35}$ (PDB ID: 1QWP). Left, predicted binding pose; right, key intermolecular interactions. (**C**) RMSD of the $A\beta_{1\text{-}42}$ backbone and **4** during 100 ns MD simulations. (**D**) Calculated binding free-energy profiles over the 100 ns simulations. Data are presented as mean ± s.d. from three independent simulation replicates. (**E**) Per-residue decomposition of the calculated binding free energy for $A\beta_{1\text{-}42}$, highlighting residues contributing to the predicted interaction with **4**.

Complex 4 attenuates AChE-facilitated amyloid assembly

Because Aβ assembly can be influenced by accessory proteins that accelerate fibrillogenesis, we next examined whether **4** could interact with the PAS of AChE, which has been implicated in promoting Aβ aggregation [31, 32]. The ligand-dependent differences in predicted docking scores were more pronounced for AChE than for Aβ. Complexes **1-4** yielded docking scores of -9.5, -9.5, -10.1, and -10.9 kcal mol^{-1}, respectively (Figures 3A and S20). **4** was predicted to occupy a region

near the PAS, where the docking analysis identified hydrogen-bonding interactions with Asp72, Asp285 and Gly335, together with π-associated contacts involving Trp279, Tyr70 and Tyr334. Additional noncovalent contacts were observed with residues including Tyr121 and Leu358. Compared with the other complexes, **4** exhibited a broader range of predicted interactions within the AChE binding environment, consistent with its more favorable docking score. These findings suggest that the extended aromatic framework of dppz may contribute to its interaction with AChE. Subsequent MD simulations showed that **4** remained associated with the predicted binding region throughout the simulation, without substantial changes in the overall protein conformation (Figures 3B-D and S21A-E). To determine whether these predicted interactions were accompanied by functional inhibition of AChE, we next examined the effects of complexes **1-4** on enzyme activity. Donepezil, an established clinical AChE inhibitor, was included as a reference compound under the same assay conditions. Biochemical assays showed that all four Ru(II) complexes inhibited AChE activity, with **4** exhibiting an IC_{50} of 6.44 ± 1.58 μM (Figure 3E,F). Complex **3** exhibited a slightly lower IC_{50}, whereas **4** retained appreciable AChE inhibitory activity alongside its effects on Aβ assembly. Donepezil inhibited AChE with an IC_{50} of 0.02 μM, demonstrating substantially greater potency than **4** under the same assay conditions [37]. Further kinetic analysis showed concentration-dependent changes in AChE activity in the presence of the complexes (Figure S22). However, the available kinetic data did not permit an unequivocal distinction between inhibition mechanisms; therefore, no definitive inhibition mechanism was assigned to complexes **1-4**.

We next examined whether **4** could attenuate AChE-facilitated Aβ aggregation [38]. Addition of AChE increased ThT fluorescence to approximately 156.14% of that observed for Aβ alone (Figure 3G), consistent with enhanced formation of ThT-positive assemblies. **4** reduced ThT fluorescence both in the absence and presence of AChE, whereas donepezil produced little change in the Aβ-only condition but partially attenuated the increase associated with AChE. In the presence of AChE, **4** reduced ThT fluorescence from approximately 156.14% to 32.24% of the Aβ-only control, indicating attenuation of AChE-facilitated Aβ assembly. To further examine changes in Aβ aggregate populations, samples were analyzed using the conformation-sensitive A11 and OC antibodies. Immunoblotting revealed reduced A11- and OC-reactive signals following treatment with **4** (Figure 3H), consistent with changes in oligomer-associated and fibrillar conformational epitopes. Together, the enzyme inhibition, aggregation, and immunochemical results indicate that **4** attenuates AChE-facilitated Aβ assembly while also affecting Aβ aggregation in the absence of AChE (Figure 3I).

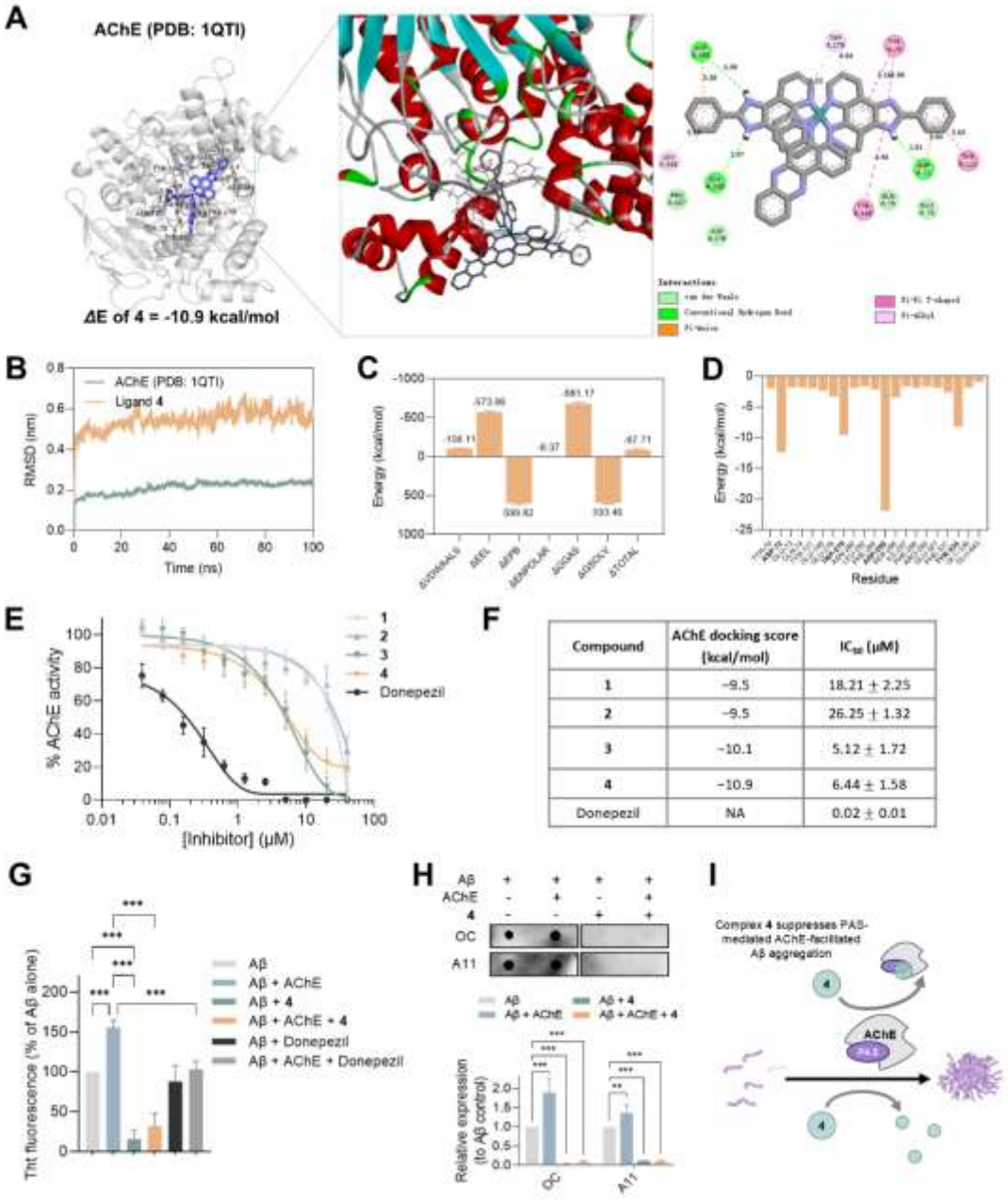

Figure 3. AChE inhibition and attenuation of AChE-facilitated Aβ aggregation by 4. (**A**) Predicted binding pose (left) and key interactions (right) of **4** with AChE (PDB: 1QTI). (**B**) Backbone and ligand RMSD during 100 ns MD simulations of the AChE-**4** complex. (**C**) Calculated binding free-energy profile during MD simulations. (**D**) Per-residue binding free-energy decomposition highlighting key AChE residues. (**E**) Concentration-dependent AChE inhibition by **1-4** and donepezil. (**F**) Summary of AChE molecular docking scores and experimentally determined IC_{50} values for complexes **1-4** and donepezil. The experimentally determined IC_{50} of donepezil was also compared with the previously reported value from reference [37]. (**G**) ThT fluorescence of Aβ incubated with or without AChE, **4**, and donepezil for 72 h, normalized to Aβ alone. (**H**) Representative Aβ dot blots probed with OC (fibrillar conformations) and A11 (prefibrillar oligomeric conformations) antibodies (top), with corresponding signal

quantification (bottom). (**I**) Schematic of PAS-associated AChE-facilitated Aβ aggregation and its attenuation by **4**. Data are mean ± s.d. from three independent experiments. Statistical significance was determined by one-way ANOVA: *P < 0.05, **P < 0.01 and ***P < 0.001.

Complex 4 shows amyloid-responsive luminescence in neuronal models

To further examine its electronic structure, DFT calculations were performed. Compared with **1-3**, **4** possesses a more extended aromatic framework (Figure S23A,B), with the calculated HOMO primarily localized on the PIP ligands and the LUMO predominantly distributed over the dppz ligand (Figure S23C). Given the characteristic MLCT emission of **4** (Figure 4A) and its sensitivity to the local molecular environment, we next examined its photophysical behavior in the presence of different Aβ assembly states to evaluate its amyloid-responsive luminescence. **4** exhibited relatively weak emission in aqueous solution, which increased upon exposure to Aβ assemblies, with the strongest response observed for fibrillar Aβ. The addition of Aβ fibrils induced changes in the absorption spectrum and enhanced the emission intensity (Figure 4B; Figure S24). The emission intensity in the presence of fibrillar Aβ was approximately twice that observed with monomeric or oligomeric Aβ (Figure 4C). Furthermore, increasing concentrations of Aβ fibrils produced a corresponding increase in emission intensity (Figure 4D), demonstrating a concentration-dependent luminescence response. These spectral changes are consistent with changes in the local molecular environment of 4 upon association with Aβ assemblies. To assess whether this response was preferential toward Aβ fibrils, **4** was further evaluated in the presence of α-synuclein, BSA, and HSA under the same experimental conditions. The emission enhancement was greatest with fibrillar Aβ (1.99-fold), followed by α-synuclein (1.73-fold), BSA (1.30-fold), and HSA (1.22-fold) (Figure 4E). These findings demonstrate a preferential luminescence response to fibrillar Aβ among the proteins examined, although the relatively modest difference compared with α-synuclein indicates that **4** does not exhibit Aβ-specific optical recognition.

The enhanced luminescence response of **4** in the presence of Aβ fibrils prompted us to investigate its potential application in amyloid-associated imaging in neuronal models. RA-differentiated SH-SY5Y and HT22 neuronal cells were used as model systems. Differentiation of SH-SY5Y cells was assessed by Western blot analysis of the neuronal markers TUJ1 and NeuN (Figure S25A). Cytotoxicity assays showed that **4** was relatively well tolerated at the concentrations examined, with 48-h IC_{50} values exceeding 50 μM in both SH-SY5Y and HT22 cells, whereas **2** and **3** produced more pronounced reductions in cell viability (Figure S25B,C). Most importantly, biologically relevant concentrations of **4** (10 μM) were well tolerated by RA-differentiated SH-SY5Y cells, even after prolonged exposure (7 days, Figure S25B,C). Confocal microscopy and SIM revealed intracellular uptake of **1-4**, with MLCT signals predominantly distributed in the cytoplasm of SH-SY5Y cells (Figure S26A,B). To examine the spatial relationship between **4** and intracellular Aβ, its luminescence distribution was further assessed in Aβ-treated neuronal cells. **4** showed partial colocalization with intracellular Aβ-positive structures (Figure 4F; Figure S27A), consistent with an association between its fluorescence distribution and Aβ-containing regions. To investigate whether **4** could also label amyloid deposits in pathological tissue, its staining properties were examined in *ex vivo* brain sections from APP/PS1 transgenic mice. **4** labelled plaque-like structures that showed substantial spatial overlap with Aβ antibody staining and ThS fluorescence (Figure 4G; Figure S27B). These observations support the potential application of **4** for amyloid-associated fluorescence imaging in cellular and tissue models.

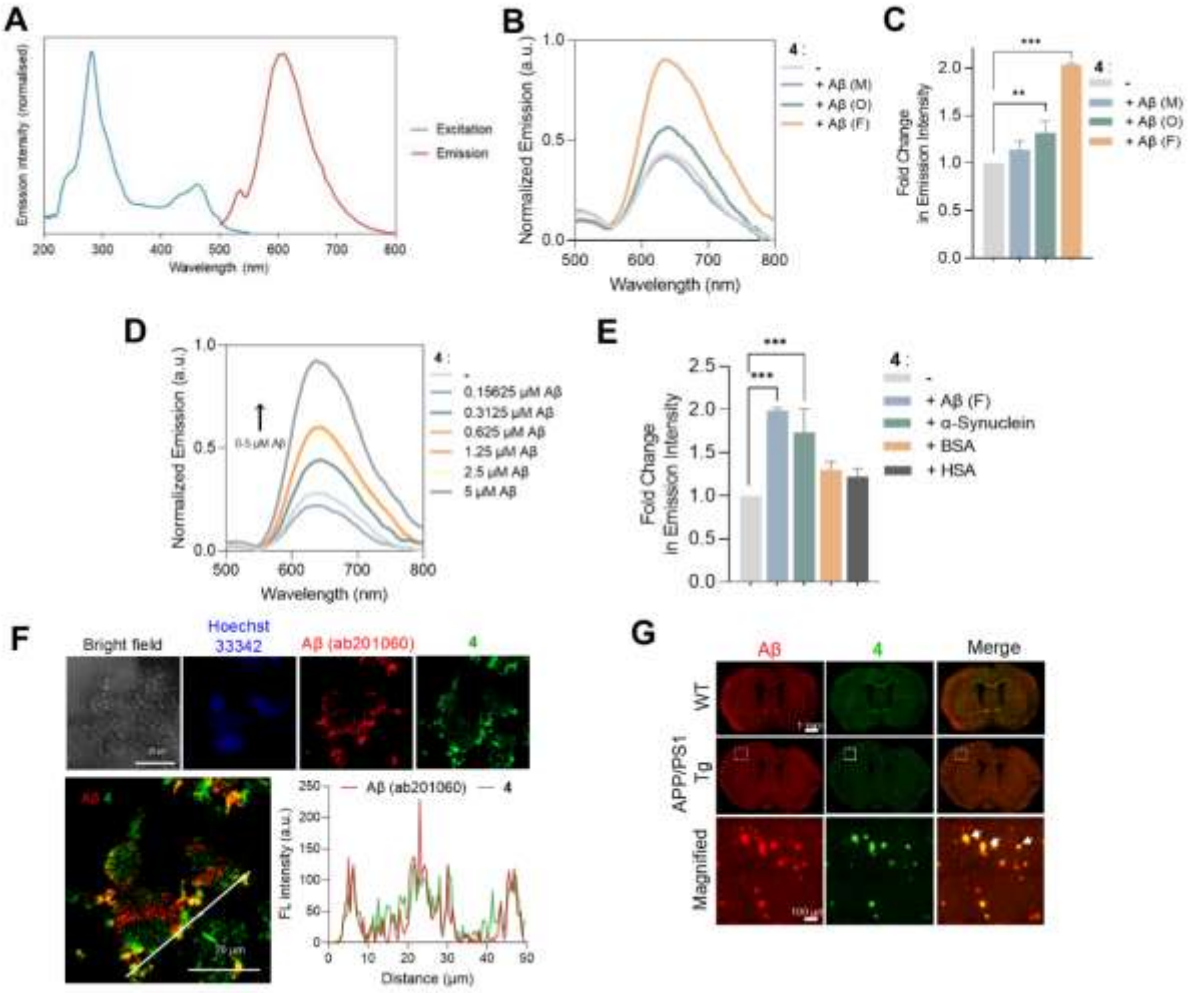

Figure 4. Amyloid-responsive luminescence of 4 enables fluorescence imaging of Aβ assemblies. (**A**) Excitation (blue; λem = 600 nm) and emission (red; λex = 450 nm) spectra of **4** (10 μM in H_2O containing 0.1% DMSO). (**B**) Emission spectra of **4** (1 μM) with Aβ monomers (M), oligomers (O), or fibrils (F) (5 μM; λex = 450 nm). (**C**) Emission intensity at 600 nm in the presence of different Aβ assemblies. (**D**) Emission spectra of **4** with increasing Aβ fibril concentrations (0-5 μM). (**E**) Emission intensity at 600 nm in the presence of Aβ fibrils, α-synuclein, BSA, or HSA. (**F**) Confocal images of SH-SY5Y cells pretreated with aggregated Aβ and stained with **4** (green), anti-Aβ antibody (red; ab201060), and Hoechst 33342 (blue). Excitation of **4**, 488 nm; emission, 580-640 nm. Scale bars, 20 μm. (**G**) Confocal images of APP/PS1 mouse brain sections stained with **4** (green) and anti-Aβ antibody (red; ab201060). Scale bars, as indicated. Quantitative data are mean ± s.d. from three independent experiments, each with three technical replicates. *P < 0.05, **P < 0.01 and ***P < 0.001 (one-way ANOVA).

Complex 4 translates amyloid engagement into neuronal protection

After establishing amyloid modulation and reporting, subsequent experiments tested whether **4** mitigates Aβ-associated neuronal injury. Neurotoxicity associated with Aβ, primarily driven by soluble Aβ oligomers, leads to neuronal atrophy and cell death. In neuronal models exposed to pre-aggregated Aβ oligomers, **4** significantly improved neuronal viability, as demonstrated by MTT and live/dead assays, and importantly preserved long-term clonogenic survival following Aβ exposure (Figure 5A-C). For example, in SH-SY5Y cells exposed to pre-aggregated Aβ oligomers, **4** markedly improved cell viability from 60.7% to 92.5%, as assessed by MTT assay. This protective effect was further supported by Calcein AM/PI staining, which showed increased Calcein AM fluorescence compared with Aβ-treated cells, and by clonogenic assays, in which colony formation increased from 20% in Aβ-treated cells to 79% following treatment with **4**. Intracellular ThT imaging further revealed a reduction in Aβ-associated ThT-positive signal in treated cells, consistent with modulation of intracellular amyloid-like aggregation (Figure 5D). Because Aβ oligomers are known to induce oxidative stress and mitochondrial dysfunction that ultimately trigger neuronal apoptosis, the analysis next examined whether **4** could mitigate these downstream pathological events.

Mechanistically, **4** attenuated Aβ-induced ROS accumulation, reduced oxidative DNA damage, preserved mitochondrial membrane potential ($\Delta\Psi_m$), and suppressed activation of apoptotic signaling pathways (Figure 5E-H). Total intracellular ROS, oxidative DNA damage, and mitochondrial integrity were evaluated using 2',7'-dichlorofluorescin diacetate (DCFH-DA), 8-oxo-dG, and tetramethylrhodamine methyl ester (TMRM) probes, respectively. Compared with Aβ-treated cells, **4** markedly reduced DCF fluorescence from 20.98-fold to 3.71-fold relative to the untreated control, indicating lower intracellular ROS levels, while increasing TMRM fluorescence intensity from 0.64-fold to 0.95-fold of the control, consistent with recovery of mitochondrial membrane potential. Western blot analysis further revealed partial normalization of the Bax/Bcl-2 ratio (1.31-fold to 1.11-fold), reduced caspase-3 activation (9.81-fold to 4.70-fold) and PARP1 cleavage (2.61-fold to 0.89-fold), together with increased expression of neuronal markers TUJ1 (0.95-fold to 1.22-fold) and NeuN (0.74-fold to 1.45-fold) relative to the untreated control (Figure 5H-J). These changes were accompanied by preservation of AKT signaling, a major pathway involved in neuronal survival. Thus, modulation of Aβ assembly by **4** was accompanied by reduced oxidative stress, preservation of mitochondrial integrity, and attenuation of apoptotic signaling pathways associated with neuronal degeneration.

Importantly, DPPH radical-scavenging assays performed in a cell-free system revealed only modest intrinsic antioxidant activity under comparable conditions (Figure S28). Although DPPH assays do not fully reproduce intracellular redox environments, the limited radical-scavenging capacity observed suggests that the reduction in intracellular ROS is unlikely to arise from direct antioxidant activity, but instead reflects mitigation of Aβ-induced oxidative stress pathways. Because three-dimensional neuronal spheroids better recapitulate tissue architecture and diffusion barriers present in the brain, the protective effects of **4** were next examined in SH-SY5Y spheroid models. **1**-**4** readily penetrated throughout the spheroid volume while retaining luminescence (Figure S29A-E). Moreover, treatment with **4** protected spheroids from Aβ-induced toxicity, as assessed by live/dead staining (Figure S29F), indicating that the Ru(II) scaffold remains bioavailable and bioactive within dense neuronal assemblies.

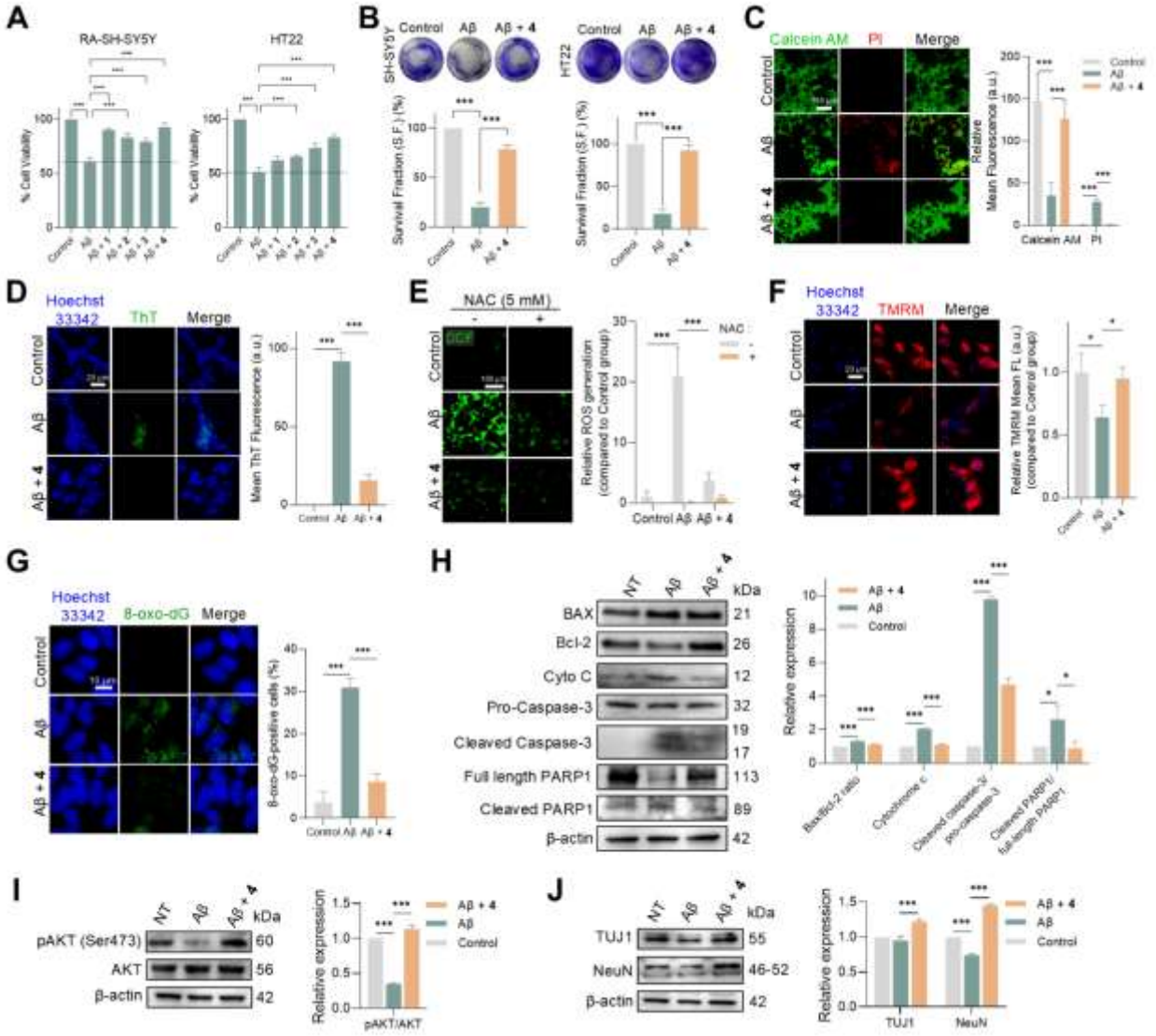

Figure 5. Complex 4 preserves neuronal homeostasis following Aβ challenge. (**A**) Viability of RA-differentiated SH-SY5Y and HT22 cells treated with preaggregated Aβ oligomers (20 μM) and **1-4** (10 μM). (**B**) Clonogenic survival of SH-SY5Y and HT22 cells treated with Aβ (20 μM) and/or **4** (10 μM) for 24 h. (**C**) Live/dead staining of RA-differentiated SH-SY5Y cells treated with Aβ (20 μM) with or without **4** (10 μM) for 24 h. Calcein-AM, green; PI, red. Scale bar, 100 μm. (**D**) ThT staining of intracellular Aβ-associated amyloid-like aggregates in RA-differentiated SH-SY5Y cells treated with preaggregated Aβ (20 μM) with or without **4** (10 μM) for 24 h. Nuclei were stained with Hoechst 33342 (blue). Scale bar, 20 μm. (**E**) Intracellular ROS levels, with NAC as an antioxidant control. Scale bar, 100 μm. (**F**) Mitochondrial membrane potential ($\Delta\Psi_m$) assessed by TMRM staining (red). Scale bar, 20 μm. (**G**) Immunofluorescence staining of 8-oxo-dG (red). Scale bar, 10 μm. Nuclei in (**F, G**) were counterstained with Hoechst 33342 (blue). (**H-J**) Western blot analysis of apoptosis-related proteins (Bax, Bcl-2, cytochrome c, procaspase-3, cleaved caspase-3, full-length and cleaved PARP1), AKT signaling (p-AKT and total AKT), and

neuronal markers (NeuN and TUJ1), respectively. β-Actin served as the loading control. Representative blots (left) and protein quantification (right). Data are mean ± s.d. from three independent experiments. Statistical significance was determined by one-way ANOVA: *P < 0.05, **P < 0.01, and ***P < 0.001.

Complex 4 attenuates Aβ-associated microglial activation

Since microglial activation contributes to the inflammatory response associated with Aβ pathology, we next examined whether **4** affected the response of BV2 microglial cells to Aβ. Aβ treatment increased Iba1 immunofluorescence approximately 3.00-fold compared with untreated cells (3.00 ± 0.74 vs. 1.00 ± 0.11; Figure 6A). This increase was markedly attenuated following treatment with **4**, with Iba1 fluorescence decreasing to 1.17 ± 0.14. In contrast, **4** alone produced an Iba1 fluorescence intensity of 1.07 ± 0.08, comparable to the untreated control. Consistent with the increased Iba1 signal, Aβ exposure also elevated the levels of the pro-inflammatory cytokines TNF-α and IL-1β in BV2 culture supernatants (Figure 6B,C). TNF-α levels increased from 288.03 ± 32.15 pg/mL in control cells to 546.85 ± 24.99 pg/mL following Aβ exposure, whereas treatment with **4** reduced these levels to 420.04 ± 19.79 pg/mL. Similarly, IL-1β levels increased from 13.67 ± 0.67 pg/mL to 22.25 ± 0.45 pg/mL following Aβ treatment and decreased to 17.08 ± 2.32 pg/mL in the presence of **4**. Together, these findings suggest that **4** attenuates Aβ-associated increases in Iba1 immunofluorescence and reduces pro-inflammatory cytokine release in BV2 microglial cells.

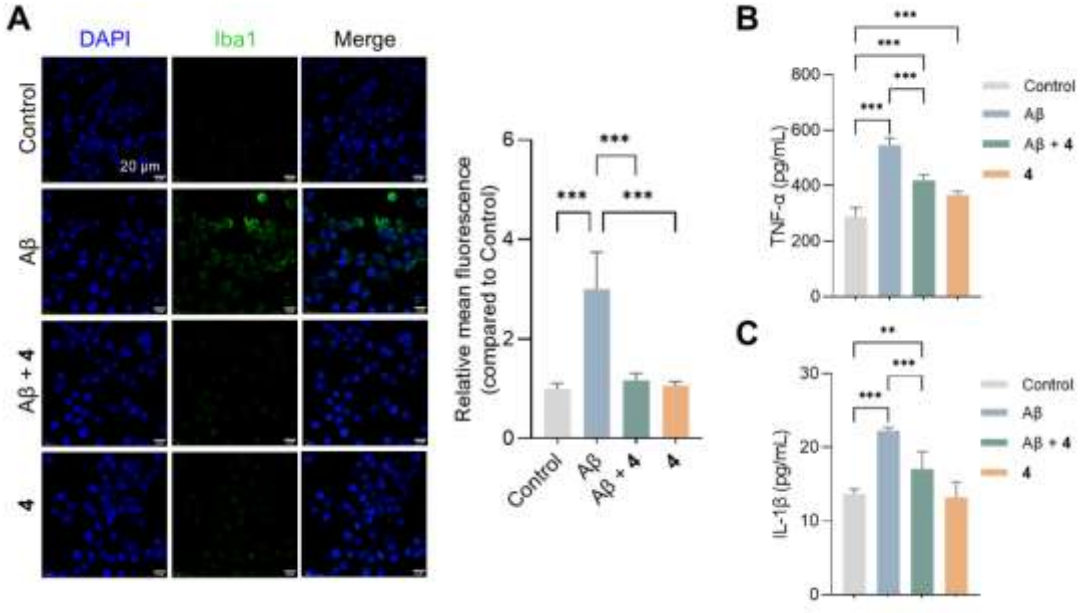

Figure 6. Complex 4 attenuates Aβ-associated inflammatory responses in BV2 microglial cells. (**A**) Immunofluorescence analysis of Iba1 expression in BV2 microglial cells treated with Aβ and/or **4** for 24 h. Left, representative fluorescence images; right, quantification of Iba1

fluorescence intensity. Nuclei were counterstained with DAPI (blue). Scale bars, 20 μm. (**B,C**) ELISA quantification of TNF-α (**B**) and IL-1β (**C**) levels in culture supernatants collected from BV2 cells following the treatments described in (**A**). Data are presented as mean ± s.d. from three independent experiments. Statistical significance was determined by one-way ANOVA: *P < 0.05, **P < 0.01, and ***P < 0.001.

Complex 4 reduces persistent amyloid burden and neural dysfunction *in vivo*

Zebrafish provide an established vertebrate model for investigating Aβ-associated neurotoxicity, amyloid deposition, and functional abnormalities within an intact nervous system [39, 40]. Previous studies have demonstrated that intracerebral administration of Aβ induces amyloid-associated pathological changes and behavioral impairments, providing a useful experimental platform for evaluating amyloid-modulating interventions [41-43]. Although several experimental compounds have been investigated using zebrafish models of Aβ-associated neurotoxicity, the *in vivo* biological activities of metal-based amyloid modulators remain less extensively characterized. We therefore employed an intracerebral Aβ-injection model to investigate whether the aggregation-modulating effects of **4** observed *in vitro* were accompanied by reduced amyloid-associated pathology, neuronal injury, and functional impairment *in vivo*. In this model, **4** was administered 4 h after Aβ injection to assess its effects following initial Aβ exposure. Direct intracerebral administration enabled evaluation of the compound's activity within the central nervous system without requiring blood-brain barrier transport. To first examine the distribution and retention of **4** in brain tissue, 3-day-post-fertilization (dpf) zebrafish larvae were intracerebrally injected with **4**, and whole-mount confocal imaging was performed at 1, 72, and 120 h. The spatial distribution of the luminescence signal was evaluated by quantifying the fluorescence-positive area. Imaging at these timepoints revealed progressive distribution of **4** from the injection site into surrounding brain tissue (dorsal view, Figure 7A,B; lateral view, Figure S30A,B), whereas no intrinsic fluorescence was observed in control larvae. ICP-MS analysis further confirmed the presence of ruthenium in larval head tissue with an average content of 0.02 ng per larval head at 24 h (Figure 7C). No lethality was observed following treatment with **4** (up to 10 mM, data not shown).

An intracerebral Aβ injection model was established in 3 dpf zebrafish larvae to enable localized amyloid deposition and real-time monitoring of peptide dynamics and complex distribution (schematic representation of the study, Figure 7D). No lethality was observed following Aβ injection (50 μM per larva, data not shown). To monitor amyloid distribution *in vivo*, HiLyte Fluor 647-labelled $A\beta_{1–42}$ was injected into the cerebroventricular space. Partial spatial colocalization between Aβ-associated fluorescence and **4** luminescence was observed in the larval brain (Figure 7E). Immunofluorescence using an anti-Aβ antibody further confirmed the presence and gradual redistribution of Aβ-associated signal within the larval brain (Figure S30C,D). To assess the effect of **4** on Aβ-associated pathology, larvae were first intracerebrally injected with $A\beta_{1-42}$, followed by administration of **4** or vehicle after a 4 h incubation period, allowing initial aggregate formation prior to treatment. Imaging was then performed at 1, 72, and 120 h post-complex **4** injection (hpi) to evaluate changes in Aβ distribution. Fluorescence-positive Aβ signal was monitored over time, with fluorescence intensity used as a proxy for Aβ persistence. In PBS-injected larvae, no fluorescence signal was detected, whereas red fluorescence remained detectable in Aβ-only controls (dorsal view, Figure 7F,G; lateral view, Figure S30E,F). In contrast, treatment with **4** progressively reduced Aβ-associated fluorescence, from 10.70 to 4.27 arbitrary units at the

first measurement point, 4.70 to 0.53 at the second, and 2.89 to 0.17 at the third, compared with Aβ-only controls.

Next, oxidative stress and neurodegeneration were assessed. ROS levels were measured using DCFH-DA, and synaptophysin staining was used as an indicator of synaptic integrity. Treatment with **4** reduced Aβ-associated ROS fluorescence from 2.81 to 1.20, restored synaptophysin fluorescence from 22.91 to 37.68 arbitrary units, and decreased TUNEL-positive staining from 33.49% to 10.88% compared with Aβ-treated larvae (Figure 7H-J). Similar protective changes were observed in neuronal cell models, where **4** reduced oxidative stress, preserved mitochondrial membrane potential, and attenuated apoptotic signaling.

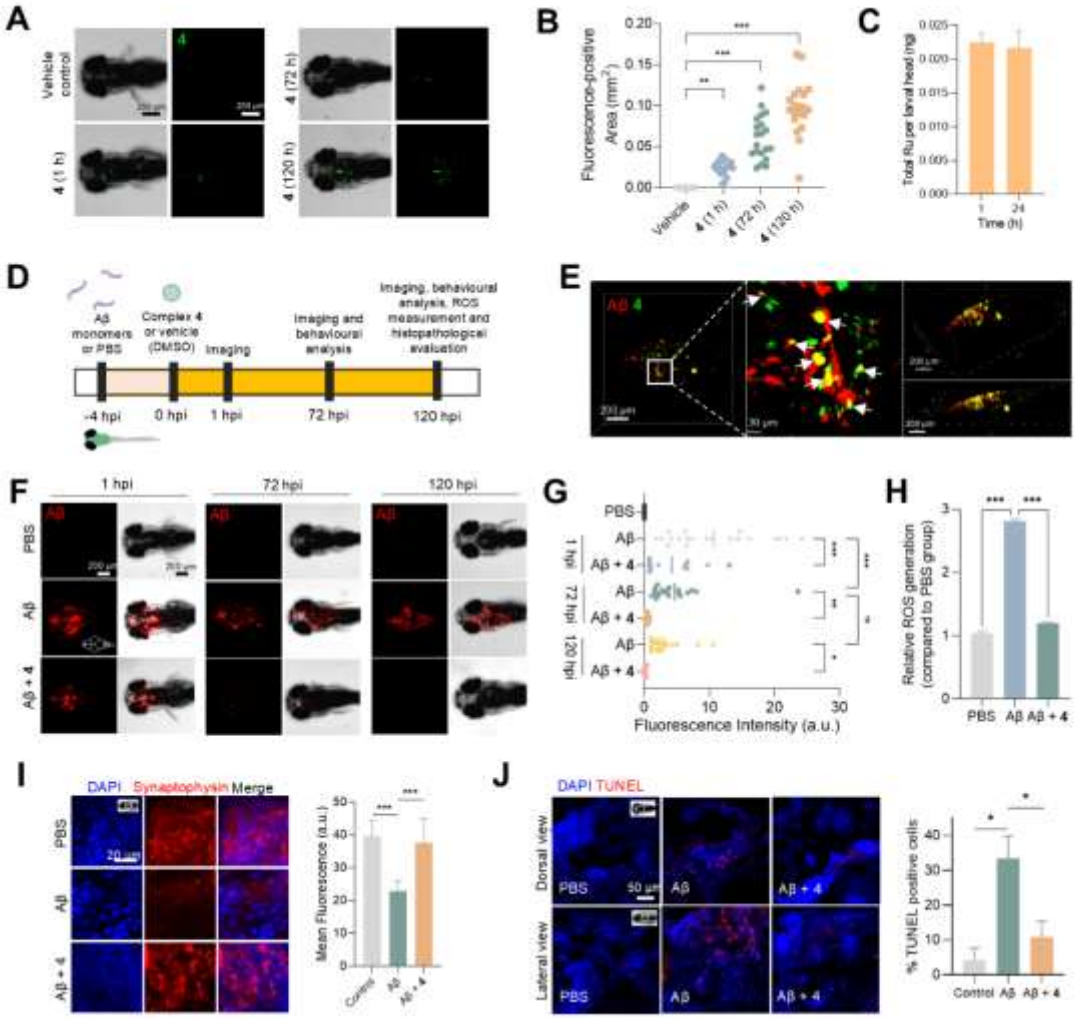

Figure 7. Effects of 4 on Aβ-associated pathology in zebrafish larvae. (**A**) Confocal images of **4** distribution in 3 dpf zebrafish larvae at 1, 72, and 120 h after intracerebral injection. Scale bars, 200 µm. (**B**) Quantification of fluorescence-positive area in the head region over time using a consistent intensity threshold. (**C**) ICP-MS quantification of Ru in larval heads at 1 and 24 h. (**D**) Experimental timeline. Larvae (3 dpf) received intracerebral $Aβ_{1-42}$-HiLyte Fluor 647 (5 nL, 50 µM), followed 4 h later by **4** (5 nL, 1 mM) or vehicle. hpi, hours post-injection of **4**. (**E**) Confocal images showing the spatial overlap of **4** and Aβ-associated fluorescence at 72 hpi. Scale bars, as

indicated. (**F**) Longitudinal confocal images of Aβ-associated fluorescence in larval brains at 1, 72, and 120 hpi (dorsal view). Scale bars, 200 μm. (**G**) Quantification of brain Aβ fluorescence intensity over time. (**H**) ROS levels in excised larval heads measured by DCFH-DA fluorescence. (**I**) Representative synaptophysin immunostaining (red) in larval brains (left) and fluorescence quantification (right). DAPI, blue. Scale bar, 20 μm. (**J**) Representative TUNEL staining (red) in larval heads (left) and quantification of TUNEL-positive cells (right). DAPI, blue. Scale bar, 50 μm. Quantitative data are mean ± s.d. For the individual-larva measurements, n = 20 larvae per group from two independent experiments (10 larvae per experiment), with each dot representing one larva. For the ICP-MS analysis in panel **C**, n = 2 independently prepared pooled samples per group, each comprising 10 larval heads (20 larvae in total per group). Statistical significance was determined by one-way ANOVA, where applicable: *P < 0.05, **P < 0.01, ***P < 0.001; ns, not significant.

Complex 4 improved Aβ-impaired locomotor behavior in larvae

To determine whether these effects translate into functional improvement, locomotor behavior was assessed using automated behavioral tracking. Spontaneous locomotion provides a measure of baseline motor activity, whereas stimulus-evoked responses assess behavioral responsiveness to external stimulation, which involves sensorimotor processing [44, 45]. Total swimming distance was defined as the cumulative distance travelled during the recording period, while mean swimming speed was calculated over the entire recording period, including periods of inactivity. Movement duration was recorded separately as the cumulative time during which movement was detected. At 3 days post-injection, no significant differences in spontaneous locomotion were observed between groups (Figure 8A and Figure S31). By 5 days post-injection, Aβ-injected larvae exhibited pronounced locomotor impairment (Figure 8B), with total swimming distance decreasing from 10,315.00 mm in PBS-injected controls to 4,395.12 mm. Treatment of Aβ-injected larvae with **4** increased swimming distance to 9,545.64 mm, accompanied by improvements in swimming speed and movement duration. Uninjected and PBS-injected larvae exhibited comparable behavioral performance, suggesting that the injection procedure itself had little effect on these locomotor parameters.

Stimulus-evoked swimming behavior, assessed by mechanical tapping (one tap every 5 s for 10 min; Figure 8C), was also impaired following Aβ injection (Figure 8D). Treatment with **4** increased total swimming distance from 336.53 to 1,102.78 mm, accompanied by improvements in swimming speed and movement duration, indicating substantial recovery of stimulus-associated locomotor activity. Treatment with **4** significantly improved responsiveness to mechanical stimulation, indicating improvement across both spontaneous and stimulus-evoked behavioral paradigms.

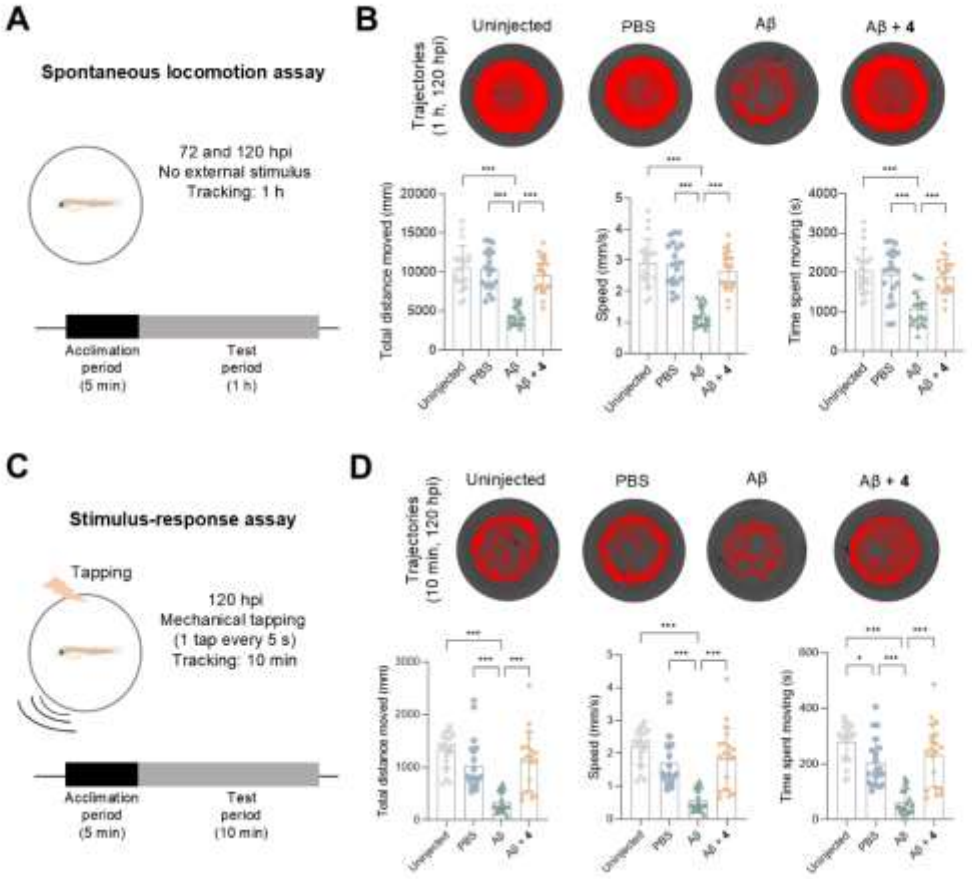

Figure 8. Effects of 4 on Aβ-associated locomotor deficits in zebrafish larvae. (**A**) Experimental timeline for spontaneous locomotor activity analysis. (**B**) Representative swimming trajectories (top) and quantification of total distance, mean speed, and movement duration (bottom) at 5 days post-injection (dpi; 1 h recording). (**C**) Schematic of the mechanical stimulus assay (one tap every 5 s for 10 min). (**D**) Representative swimming trajectories (top) and corresponding locomotor parameters (bottom) during mechanical stimulation at 5 dpi. Data are mean ± s.d. (n = 20 larvae per group from two independent experiments, 10 per experiment). Each dot represents one larva. Statistical significance was determined by one-way ANOVA: *P < 0.05, **P < 0.01, and ***P < 0.001.

Complex 4 restores locomotor and cognitive performance in adult zebrafish

While larval zebrafish provide a useful platform for visualizing amyloid dynamics, adult zebrafish possess more mature neural circuits that allow assessment of complex behavioral functions relevant to AD. To evaluate longer-term functional outcomes in a mature vertebrate nervous system, we extended our analysis to adult zebrafish. Intracerebral injection of Aβ produced pronounced behavioral deficits, including reduced swimming activity and impaired exploratory behavior compared with PBS-injected controls at both 7 and 14 days post-injection (dpi) (14 dpi, Figure 9A-C; 7 dpi, Figure S32A-C). These time points were selected to assess the progression of behavioral changes following Aβ-induced neurotoxicity. Treatment with **4**, administered 4 h after Aβ injection, ameliorated locomotor deficits in adult zebrafish, as reflected by improvements in

swimming trajectories, mean distance moved, and mean swimming speed. At 14 dpi, **4** increased the mean distance moved from 1,360.68 to 2,784.97 mm and the corresponding mean swimming speed from 22.68 to 46.42 mm/s compared with Aβ-treated fish (Figure 9C), indicating improved locomotor performance following treatment.

Cognitive performance was further evaluated using a T-maze food-reward paradigm to assess spatial learning and memory-related behavior. Fish were trained twice daily to associate a designated arm of the maze with a food reward, and their subsequent exploration of this arm was evaluated during a 6-min trial (T-maze setup, Figure 9D; training schematic, Figure S32D). At 14 dpi, Aβ-treated fish exhibited poorer T-maze performance than PBS-injected controls, with reduced cumulative time spent in the target arm, increased latency to first entry into the target arm, and fewer target-arm entries (Figure 9E,F). These behavioral differences were less apparent at 7 dpi (Figure S32E,F). Treatment with **4** improved T-maze performance at 14 dpi, as reflected by increased target-arm exploration. Together, the locomotor and T-maze findings suggest that **4** attenuates Aβ-associated behavioral impairments in adult zebrafish, extending its observed effects from molecular and cellular models to functional outcomes in a mature vertebrate nervous system.

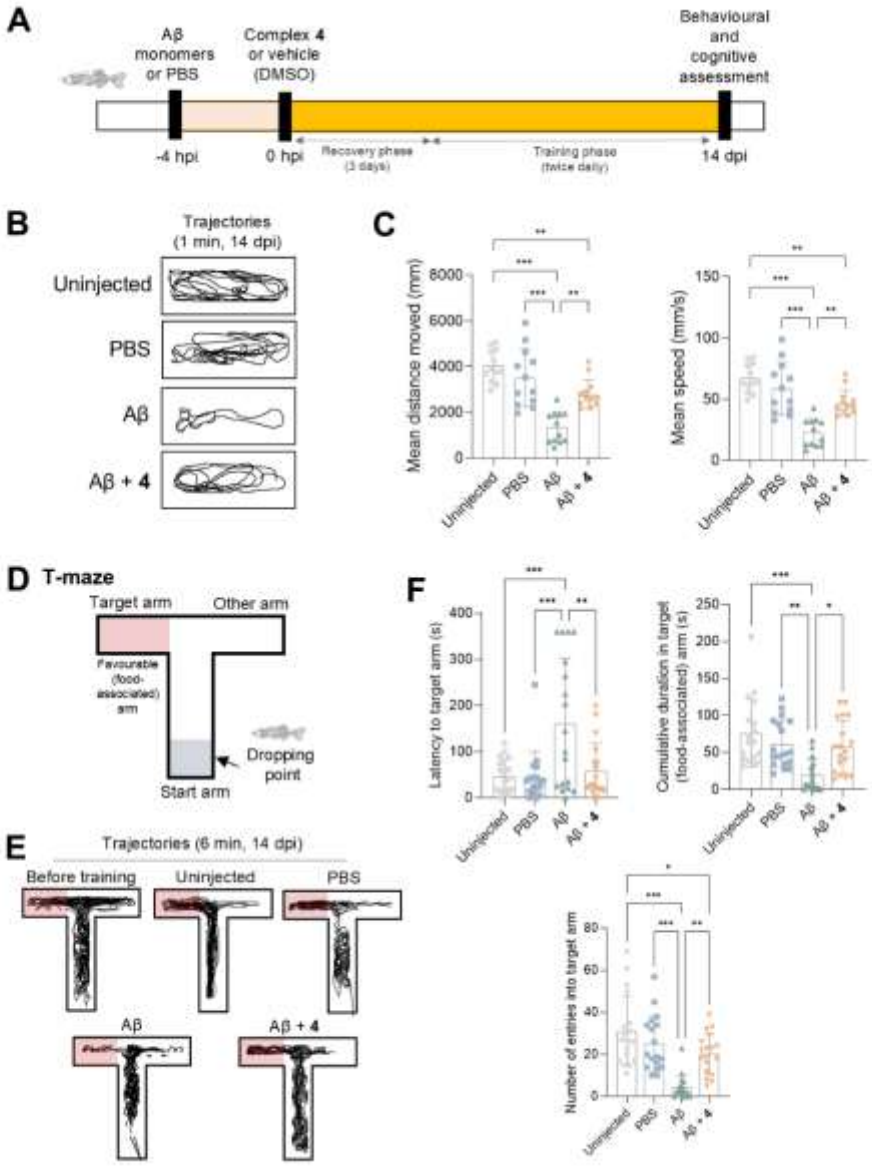

Figure 9. Effects of 4 on locomotor and cognitive performance in adult zebrafish. (**A**) Experimental timeline. Adult zebrafish received intracerebral $A\beta_{1\text{-}42}$ (100 nL, 500 µM), followed 4 h later by **4** (100 nL, 2 mM). hpi, hours post-injection of **4**; dpi, days post-injection of **4**. (**B, C**) Representative swimming trajectories (**B**) and quantification of mean distance moved (mm) and mean speed (mm/s) (**C**) at 14 dpi (1 min recording). (**D**) Schematic of the food-reward T-maze assay. Fish were trained to associate the target arm with food before memory retention testing (training protocol, Figure S32D). (**E**) Representative T-maze trajectories recorded over 6 min, selected based on proximity to the group mean. Uninjected, untrained fish served as controls. (**F**) Quantification of latency to first target-arm entry, cumulative duration in the target arm, and number of target-arm entries during the 6 min test. Data are mean ± s.d. (**C**: n = 12 fish per group from two independent experiments; **F**: n = 18 fish per group from three independent experiments). Each dot represents one fish. Statistical significance was assessed by one-way ANOVA: *P < 0.05, **P < 0.01, ***P < 0.001.

Discussion

Ruthenium(II) polypyridyl complexes have previously been investigated as amyloid-responsive probes and aggregation modulators. Cook et al. examined the photoluminescence response of $[Ru(bpy)_2(dppz)]^{2+}$ associated with Aβ, finding the complex binds to a hydrophobic cleft on the surface of Aβ fibrils between Val18 and Phe20 [20]. Yu et al. developed $[Ru(phen)_2(fipc)]^{2+}$ (fipc = 5-fluoro-N-(1,10-phenanthrolin-5-yl)-1H-indole-2-carboxamide) as a luminescent probe to monitor Aβ aggregation while Jiang et al. employed $[Ru(bpy)_2(dpqp)]^{2+}$ (dpqp = pyrazino-[2′,3′:5,6]-pyrazino-[2,3-f]-[1,10]-phenanthroline) and photoluminescence anisotropy to track the formation of amyloid oligomers [21, 23]. In these latter two cases, Aβ aggregation was not perturbed by binding, supporting the proposed use of each molecule as a non-invasive probe. Vyas et al. reported Ru complexes of general formula $[Ru(N^N)_2(txbg)]^{2+}$ (txbg = tetra-xylene bipyridine glycoluril) capable of inhibiting Aβ aggregation, as evaluated using ThT fluorescence and complementary structural analyses [25]. 100% *in vitro* Aβ aggregation inhibition was achieved after 240 h of incubation for the majority of complexes tested, including N^N = dppz, and very weak activity of these complexes against AChE was reported. However, a related study by the same group demonstrated the potential of Ru(II) complexes for both amyloid modulation and cholinesterase inhibition [46]. Similar to the above studies, we identify a substitutionally-inert RPC to bind Aβ, however, the combination of reduced fibril formation, AChE inhibition and attenuation of AChE-facilitated amyloid aggregation distinguishes **4** from previously reported complexes. Moreover, it is a significant advance on previous work that we show the complex achieves reduced Aβ-associated neuronal injury in cellular and zebrafish models, including the restoration of locomotor and cognitive performance in an AD model. Compared with the previously reported $[Ru(bpy)_2(dppz)]^{2+}$ complex, **4** incorporates two extended aromatic PIP ligands that provide additional surfaces for noncovalent interactions with Aβ. Although its predicted contacts with the central hydrophobic region of $Aβ_{1-42}$ partially overlap with those reported by Cook et al. [20], **4** also modulated the assembly of $Aβ_{25-35}$, which lacks this region. This suggests that the extended polypyridyl framework of **4** may accommodate interactions with different Aβ sequences or assembly environments, rather than relying on a single recognition region.

It is of interest that **4** exhibited greater Aβ aggregation-modulating activity than **1-3** in the experimental assays, suggesting that variations in the N,N-donor ligand influence these biological responses. The extended aromatic surface and hydrophobic character of the dppz ligand may facilitate interactions with Aβ, consistent with the proposed role of aromatic interactions in amyloid recognition and aggregation modulation [47]. Indeed, similar structure-activity relationships have been discussed for other metal-based amyloid modulators [48-53]. However, the experimental differences among **1-4** were not reflected in the predicted Aβ docking scores, which showed only modest variation across the series. In contrast, AChE docking revealed more pronounced ligand-dependent differences, with **4** exhibiting the most favorable predicted binding score. Consistent with its experimentally observed AChE inhibitory activity, **4** also attenuated the increase in Aβ-associated ThT fluorescence observed in the presence of AChE. Thus, these findings suggest that the dppz ligand contributes to the multifunctional activity of **4**, although its effects cannot be attributed solely to increased aromaticity or the predicted binding interactions. Other structural and physicochemical factors, including molecular geometry, electronic

distribution and interactions with different Aβ assembly states, may also contribute to its experimental behavior.

The limitations of the study should also be considered. The intracerebral Aβ-injection model reproduces selected features of acute Aβ-associated neurotoxicity but does not recapitulate the progressive amyloid pathology of Alzheimer's disease. Moreover, direct intracerebral administration enables evaluation of biological activity within the central nervous system but bypasses the blood-brain barrier and does not establish systemic brain delivery, long-term pharmacokinetics, or efficacy against established amyloid plaques. Furthermore, although the complementary aggregation assays indicate that **4** alters Aβ assembly, they do not fully resolve the native oligomer populations or the individual microscopic steps involved in aggregation. The luminescence response also cannot be considered exclusive to Aβ, given the response observed with other amyloid-associated protein environments. The present study should therefore be considered a vertebrate proof-of-concept for the amyloid-modulating and neuroprotective potential of **4** rather than a therapeutic validation study. Future investigations should evaluate systemic delivery approaches, including carrier-assisted transport and structural optimization for improved brain exposure, together with longer-term evaluation in mammalian models that more closely reproduce the progressive pathology of Alzheimer's disease. Further characterization of oligomerization dynamics, secondary nucleation and the relationship between Aβ assembly states and cellular toxicity would also help clarify the mechanism of action. In conclusion, this study identifies a Ru(II)-based molecular system that combines amyloid-responsive luminescence with Aβ assembly modulation and biological activity, supporting further investigation of coordination complexes for the visualization and modulation of Aβ-associated processes.

Abbreviations

AChE: Acetylcholinesterase; AD: Alzheimer’s disease; Aβ: amyloid-β; BCA: Bicinchoninic acid assay; BSA: bovine serum albumin; CLSM: confocal laser scanning microscopy; CO_2: carbon dioxide; DAPI: 4′,6-diamidino-2-phenylindole; DCFH-DA: 2’,7’-dichlorofluorescin diacetate; DFT: density functional theory; DLS: dynamic light scattering; DMEM: Dulbecco's Modified Eagle Medium; dpf: days post-fertilization; DPPH: 2,2-diphenyl-1-picrylhydrazyl; DTNB: 5,5′-dithiobis-(2-nitrobenzoic acid); FBS: fetal bovine serum; FT-IR: Fourier transform infrared spectroscopy; HFIP: hexafluoroisopropanol; HOMO: highest occupied molecular orbital; HPLC: high-performance liquid chromatography; HSA: human serum albumin; IC_{50}: half-maximal inhibitory concentration; ICP-MS: Inductively coupled plasma mass spectrometry; IL-1β: interleukin-1β; KOH: potassium hydroxide; LUMO: lowest unoccupied molecular orbital; MD: Molecular dynamics; MEM: minimum essential medium; MLCT: metal-to-ligand charge-transfer; MTT: 3-(4,5-dimethylthiazol-2-yl)-2,5-diphenyltetrazolium bromide; NAC: N-acetylcysteine; $NaHCO_3$: Sodium bicarbonate; NEAA: nonessential amino acids; NMR: Nuclear magnetic resonance; PAS: peripheral anionic site; PBS: phosphate-buffered saline; PFA: paraformaldehyde; RA: retinoic acid; Rg: radius of gyration; RMSD: Root mean square deviation; RMSF: root mean square fluctuation; ROS: Reactive oxygen species; RT: room temperature; SASA: solvent-accessible surface area; SD: standard deviation; SIM: structured illumination microscopy; TBST: Tris Buffered Saline with Tween 20; TEM: Transmission electron microscopy; ThS: Thioflavin S; ThT: Thioflavin T; TMRM: tetramethylrhodamine methyl ester; TNF-α: tumor necrosis factor-α; $\Delta\Psi m$: mitochondrial membrane potential

Acknowledgments
The authors thank the staff at West China Hospital of Sichuan University for their support, in particular Xiangyi Ren and Jian Yang from the Tianfu Life Science Park Public Platform for technical assistance with confocal imaging. The authors also thank the chemistry team members at WuXi AppTec for technical support with the synthesis and characterization of the compounds. Shenzhen Shuyan Calculation Tech Co., Ltd. is acknowledged for assistance with molecular docking calculations. The authors further thank the Beijing Qingxing Technology Research Institute for technical support with TEM, DLS and ICP-MS analysis, London Metropolitan University for elemental analysis and the National Mass Spectroscopy Facility (NMSF) at Swansea University.

Funding
This work was supported by grants from the National Natural Science Foundation of China (W2533071 to N.A.Y. and 32522029 to J.C.), the Science and Technology Department of Sichuan (2026NSFSCZY0110 to J.C.), and the 1·3·5 Project for Disciplines of Excellence at West China Hospital of Sichuan University (ZYYC24011 to X.T. and 2024HXFH035 to J.C.). M.G. acknowledges funding support from the Higher Education Council for Wales and Swansea University.

Author contributions
N.A.Y. and Y.Y. performed the experiments, analyzed the data, and prepared the figures. D.C., A.T., Y.G., and Y.C. contributed to experimental work and data collection. X.T., M.R.G., and J.C. conceived and supervised the study. N.A.Y. and M.R.G. drafted the manuscript. N.A.Y., Y.Y., X.T., M.R.G., and J.C. revised the manuscript. All authors reviewed and approved the final manuscript.

Competing interests
The authors have declared that no competing interests exist.

Data availability statement
The data that support the findings of this study are available upon reasonable request.

References
1. 2023 Alzheimer's disease facts and figures. Alzheimer's dement. 2023; 19: 1598-695.
2. Knopman DS, Amieva H, Petersen RC, Chételat G, Holtzman DM, Hyman BT, et al. Alzheimer disease. Nat Rev Dis Primers. 2021; 7: 33.
3. Hampel H, Hardy J, Blennow K, Chen C, Perry G, Kim SH, et al. The Amyloid-β Pathway in Alzheimer's Disease. Mol Psychiatry. 2021; 26: 5481-503.
4. Jia Y-J, Ge Y-J, Li B, Yang Y, Chen H, Liu J, et al. Advances in Alzheimer's disease: mechanistic insights and therapeutic targets. Sci China Life Sci. 2026; 69: 2543-74.
5. Zott B, Simon MM, Hong W, Unger F, Chen-Engerer H-J, Frosch MP, et al. A vicious cycle of β amyloid–dependent neuronal hyperactivation. Science. 2019; 365: 559-65.

6. Nirmalraj PN, List J, Battacharya S, Howe G, Xu L, Thompson D, et al. Complete aggregation pathway of amyloid β (1-40) and (1-42) resolved on an atomically clean interface. Sci Adv. 2020; 6: eaaz6014.
7. Nirmalraj PN, Bhattacharya S, Thompson D. Accelerated Alzheimer's Aβ-42 secondary nucleation chronologically visualized on fibril surfaces. Sci Adv. 2024; 10: eadp5059.
8. Albertini G, Zielonka M, Cuypers M-L, Snellinx A, Xu C, Poovathingal S, et al. The Alzheimer's therapeutic Lecanemab attenuates Aβ pathology by inducing an amyloid-clearing program in microglia. Nat Neurosci. 2026; 29: 100-10.
9. Zhang Y, Chen H, Li R, Sterling K, Song W. Amyloid β-based therapy for Alzheimer's disease: challenges, successes and future. Signal Transduct Target Ther. 2023; 8: 248.
10. Wang S, Song H, Yin C, Huo F. Advances in probe crossing the blood–brain barrier strategies and fluorescent imaging for brain dynamics. Coord Chem Rev. 2025; 543: 216940.
11. Aliyan A, Cook NP, Martí AA. Interrogating Amyloid Aggregates using Fluorescent Probes. Chem Rev. 2019; 119: 11819-56.
12. Rai H, Singh R, Shankar G, Rai S, Kumar P, Nilakhe AS, et al. Discovery of NIRF theranostic probes targeting amyloid-β and cholinesterases in Alzheimer's disease models. Nat Commun. 2026; 17: 1567.
13. Hayashi H, Saito R, Miyashita A, Ikeuchi T, Tada M, Akazawa K, et al. Expansive spatial pattern of Aβ deposition in patients with cerebral amyloid angiopathy: A three-dimensional surface-to-depth analysis. Sci Adv. 2026; 12: eaea7539.
14. Colvin MT, Silvers R, Ni QZ, Can TV, Sergeyev I, Rosay M, et al. Atomic Resolution Structure of Monomorphic Aβ42 Amyloid Fibrils. J Am Chem Soc. 2016; 138: 9663-74.
15. Chen G-f, Xu T-h, Yan Y, Zhou Y-r, Jiang Y, Melcher K, et al. Amyloid beta: structure, biology and structure-based therapeutic development. Acta Pharmacol Sin. 2017; 38: 1205-35.
16. Carroll EC, Yang H, Powell WC, Charvat AF, Oehler A, Jones JG, et al. High-throughput discovery of fluoroprobes that recognize amyloid fibril polymorphs. Nat Chem. 2025; 17: 1565-75.
17. Yasir Khan H, Ahmad A, Nadir Hassan M, Hasan Khan Y, Arjmand F, Hasan Khan R. Advances of metallodrug-amyloid β aggregation inhibitors for therapeutic intervention in neurodegenerative diseases: Evaluation of their mechanistic insights and neurotoxicity. Coord Chem Rev. 2024; 501: 215580.
18. Jiang B, Martí AA. Probing Amyloid Nanostructures Using Photoluminescent Metal Complexes. Eur J Inorg Chem. 2021; 2021: 4408-24.
19. Yusoh NA, Gill MR, Tian X. Advancing super-resolution microscopy with metal complexes: functional imaging agents for nanoscale visualization. Chem Soc Rev. 2025; 54: 3616-46.
20. Cook NP, Ozbil M, Katsampes C, Prabhakar R, Martí AA. Unraveling the Photoluminescence Response of Light-Switching Ruthenium(II) Complexes Bound to Amyloid-β. J Am Chem Soc. 2013; 135: 10810-6.
21. Yu H-j, Zhao W, Xie M, Li X, Sun M, He J, et al. Real-time monitoring of self-aggregation of β-amyloid by a fluorescent probe based on ruthenium complex. Anal Chem. 2020; 92: 2953-60.

22. Babu E, Muthu Mareeswaran P, Sathish V, Singaravadivel S, Rajagopal S. Sensing and inhibition of amyloid-β based on the simple luminescent aptamer–ruthenium complex system. Talanta. 2015; 134: 348-53.
23. Jiang B, Aliyan A, Cook NP, Augustine A, Bhak G, Maldonado R, et al. Monitoring the Formation of Amyloid Oligomers Using Photoluminescence Anisotropy. J Am Chem Soc. 2019; 141: 15605-10.
24. Singh S, Navale GR, Agrawal S, Singh HK, Singla L, Sarkar D, et al. Design and synthesis of piano-stool ruthenium(II) complexes and their studies on the inhibition of amyloid β (1–42) peptide aggregation. Int J Biol Macromol. 2023; 239: 124197.
25. Vyas NA, Ramteke SN, Kumbhar AS, Kulkarni PP, Jani V, Sonawane UB, et al. Ruthenium(II) polypyridyl complexes with hydrophobic ancillary ligand as Aβ aggregation inhibitors. Eur J Med Chem. 2016; 121: 793-802.
26. Cook NP, Kilpatrick K, Segatori L, Martí AA. Detection of α-synuclein amyloidogenic aggregates in vitro and in cells using light-switching dipyridophenazine ruthenium(II) complexes. J Am Chem Soc. 2012; 134: 20776-82.
27. Bataglioli JC, Gomes LMF, Maunoir C, Smith JR, Cole HD, McCain J, et al. Modification of amyloid-beta peptide aggregation via photoactivation of strained Ru(ii) polypyridyl complexes. Chem Sci. 2021; 12: 7510-20.
28. Son G, Lee BI, Chung YJ, Park CB. Light-triggered dissociation of self-assembled β-amyloid aggregates into small, nontoxic fragments by ruthenium (II) complex. Acta Biomater. 2018; 67: 147-55.
29. Leech G, Acosta AL, Mahato S, Barrett PC, Hodges RO, McFarland SA, et al. Photoactivatable Ru(ii) polypyridyl complexes as dual action modulators of amyloid-beta peptide aggregation and Cu redox cycling. Chem Sci. 2025; 16: 20914-23.
30. Chan TG, Ruehl CL, Morse SV, Simon M, Rakers V, Watts H, et al. Modulation of amyloid-β aggregation by metal complexes with a dual binding mode and their delivery across the blood-brain barrier using focused ultrasound. Chem Sci. 2021; 12: 9485-93.
31. Inestrosa NC, Alvarez A, Pérez CA, Moreno RD, Vicente M, Linker C, et al. Acetylcholinesterase accelerates assembly of amyloid-beta-peptides into Alzheimer's fibrils: possible role of the peripheral site of the enzyme. Neuron. 1996; 16: 881-91.
32. Alvarez A, Opazo C, Alarcón R, Garrido J, Inestrosa NC. Acetylcholinesterase promotes the aggregation of amyloid-β-peptide fragments by forming a complex with the growing fibrils. J Mol Biol. 1997; 272: 348-61.
33. Zhang J, Zhang Y, Wang J, Xia Y, Zhang J, Chen L. Recent advances in Alzheimer's disease: mechanisms, clinical trials and new drug development strategies. Signal Transduct Target Ther. 2024; 9: 211.
34. Elgar CE, Yusoh NA, Tiley PR, Kolozsvári N, Bennett LG, Gamble A, et al. Ruthenium(II) Polypyridyl Complexes as FRET Donors: Structure- and Sequence-Selective DNA-Binding and Anticancer Properties. J Am Chem Soc. 2023; 145: 1236-46.
35. Crescenzi O, Tomaselli S, Guerrini R, Salvadori S, D'Ursi AM, Temussi PA, et al. Solution structure of the Alzheimer amyloid β-peptide (1–42) in an apolar microenvironment. Eur J Biochem. 2002; 269: 5642-8.
36. Aleström P, D'Angelo L, Midtlyng PJ, Schorderet DF, Schulte-Merker S, Sohm F, et al. Zebrafish: Housing and husbandry recommendations. Lab Anim. 2020; 54: 213-24.

37. Camps P, Formosa X, Galdeano C, Gómez T, Muñoz-Torrero D, Scarpellini M, et al. Novel Donepezil-Based Inhibitors of Acetyl- and Butyrylcholinesterase and Acetylcholinesterase-Induced β-Amyloid Aggregation. J Med Chem. 2008; 51: 3588-98.
38. Bartolini M, Bertucci C, Cavrini V, Andrisano V. β-Amyloid aggregation induced by human acetylcholinesterase: inhibition studies. Biochem Pharmacol. 2003; 65: 407-16.
39. Saleem S, Kannan RR. Zebrafish: an emerging real-time model system to study Alzheimer's disease and neurospecific drug discovery. Cell Death Discov. 2018; 4: 45.
40. Kotova MM, Stewart AM, Grigoryan A, Shariff S, Mirzaei F, Kantawala B, et al. Towards Better and More Valid Zebrafish Models of Alzheimer's Disease: A Scientific Tribute to Prof. Mikhail I. Aghajanov. J Neurochem. 2025; 169: e70090.
41. Javed I, Peng G, Xing Y, Yu T, Zhao M, Kakinen A, et al. Inhibition of amyloid beta toxicity in zebrafish with a chaperone-gold nanoparticle dual strategy. Nat Commun. 2019; 10: 3780.
42. Javed I, Zhang Z, Adamcik J, Andrikopoulos N, Li Y, Otzen DE, et al. Accelerated Amyloid Beta Pathogenesis by Bacterial Amyloid FapC. Adv Sci. 2020; 7: 2001299.
43. Saleem S, Banerjee R, Rajesh Kannan R. Chrysin-Loaded Chitosan Nanoparticle-Mediated Neuroprotection in Aβ1–42-Induced Neurodegenerative Conditions in Zebrafish. ACS Chem Neurosci. 2022; 13: 2017-34.
44. Dimakou A, Pezzulo G, Zangrossi A, Corbetta M. The predictive nature of spontaneous brain activity across scales and species. Neuron. 2025; 113: 1310-32.
45. Carbo-Tano M, Lapoix M, Jia X, Thouvenin O, Pascucci M, Auclair F, et al. The mesencephalic locomotor region recruits V2a reticulospinal neurons to drive forward locomotion in larval zebrafish. Nat Neurosci. 2023; 26: 1775-90.
46. Vyas NA, Bhat SS, Kumbhar AS, Sonawane UB, Jani V, Joshi RR, et al. Ruthenium(II) polypyridyl complex as inhibitor of acetylcholinesterase and Aβ aggregation. Eur J Med Chem. 2014; 75: 375-81.
47. Porat Y, Abramowitz A, Gazit E. Inhibition of amyloid fibril formation by polyphenols: structural similarity and aromatic interactions as a common inhibition mechanism. Chem Biol Drug Des. 2006; 67: 27-37.
48. Skeby KK, Sørensen J, Schiøtt B. Identification of a common binding mode for imaging agents to amyloid fibrils from molecular dynamics simulations. J Am Chem Soc. 2013; 135: 15114-28.
49. Man BY-W, Chan H-M, Leung C-H, Chan DS-H, Bai L-P, Jiang Z-H, et al. Group 9 metal-based inhibitors of β-amyloid (1–40) fibrillation as potential therapeutic agents for Alzheimer's disease. Chem Sci. 2011; 2: 917-21.
50. Barnham KJ, Kenche VB, Ciccotosto GD, Smith DP, Tew DJ, Liu X, et al. Platinum-based inhibitors of amyloid-β as therapeutic agents for Alzheimer's disease. Proc Natl Acad Sci USA. 2008; 105: 6813-8.
51. La Manna S, Di Natale C, Panzetta V, Leone M, Mercurio FA, Cipollone I, et al. A Diruthenium Metallodrug as a Potent Inhibitor of Amyloid-β Aggregation: Synergism of Mechanisms of Action. Inorg Chem. 2024; 63: 564-75.
52. Wall BJ, Will MF, Yawson GK, Bothwell PJ, Platt DC, Apuzzo CF, et al. Importance of Hydrogen Bonding: Structure–Activity Relationships of Ruthenium(III) Complexes with Pyridine-Based Ligands for Alzheimer's Disease Therapy. J Med Chem. 2021; 64: 10124-38.

53. Huffman SE, Yawson GK, Fisher SS, Bothwell PJ, Platt DC, Jones MA, et al. Ruthenium(iii) complexes containing thiazole-based ligands that modulate amyloid-β aggregation. Metallomics. 2020; 12: 491-503.